The role of glauconite content in controlling sand crushing and compressibility

Shijin Li[1], Hannes Claes[2], Hadrien Rattez[3]

Shijin Li, PhD, [1] Institute of Mechanics, Materials and Civil Engineering, Université Catholique de Louvain, Louvain-la-Neuve, B-1348, Belgium. shijin.li@uclouvain.be. https://orcid.org/0000-0002-2918-3934

Hannes Claes, [2] Department of Earth and Environmental Sciences, Geology, KU Leuven, 3001 Leuven, Belgium. hannes.claes1@kuleuven.be. https://orcid.org/0000-0002-2424-6975.

Hadrien Rattez, [3] Institute of Mechanics, Materials and Civil Engineering, Université Catholique de Louvain, Louvain-la-Neuve, B-1348, Belgium. hadrien.rattez@uclouvain.be. https://orcid.org/0000-0002-7245-6563.

* (Corresponding author) Email: hadrien.rattez@uclouvain.be

Please note that this manuscript has been submitted for publication and is currently under peer review.

Figures: 21 (please refer to figure files for higher quality versions)

Tables: 2

Main text word count: 7698

ABSTRACT

Glauconite-rich sands are increasingly posing engineering challenges in offshore and nearshore developments, since their mechanical behaviour remains poorly understood owing to the extreme crushability of glauconite grains. Particle crushing in these sediments alters stiffness, compressibility, grading, particle morphology and, consequently, engineering performance. This study presents a comprehensive experimental programme to quantify the crushability of two types of pure glauconite, glauconite-silica mixtures, and silica sand under one-dimensional oedometric compression. Loading-unloading oedometer tests arrested at different axial strains were conducted on five materials containing varying glauconite, in both dry and saturated conditions. High-resolution laser diffraction and dynamic image analysis were used to characterise the evolutions of particle size and shape. The results show that glauconite exhibits substantially lower yield stress and requires far less work input to initiate crushing than silica sand. Yielding stress and threshold work decrease nonlinearly with increasing glauconite content, while relative breakage grows approximately linearly with strain. All materials evolve toward finer, fractal particle size distributions, and a robust exponential relationship between relative breakage and fractal dimension is established. Shape analysis reveals progressive elongation and edge irregularity with breakage, with glauconite retaining more equant geometries compared with silica. By integrating stress-strain behaviour, energy dissipation, grading evolution, and particle-shape change, this work presents a unified experimental framework for understanding crushing of glauconitic sands. The results support improved foundation design, breakage-aware constitutive modelling, and assessments of construction (e.g., pile installation) and long-term performance in glauconite-rich deposits.

Keywords: Glauconite; oedometer test; crushing; particle size distribution; particle shape evolution

Highlights

- Glauconite content significantly reduces yield stress and crushing work input.
- Water reduces glauconite yield stress by 88.2%, inducing clay-like behaviour.
- A robust exponential relationship links relative breakage to fractal dimension.
- Glauconite retains more equant grain shapes during breakage than silica sand.

1. Introduction

Glauconite is a green, iron-potassium phyllosilicate mineral that forms predominantly in shallow marine environments, typically appearing as small rounded pellets that impart the characteristic green colour of "greensands" (Tedrow, 2002). Because of their weak, brittle, and micro-porous internal structure, glauconite grains crush readily under relatively low stresses, causing the material to rapidly transform from a stiff, permeable coarse-grained sand into a weak, low-permeability fine-grained soil. Such transformations are increasingly recognised as a key challenge in nearshore and offshore geotechnical engineering, particularly along shallow marine shelves where wind farm developments are expanding rapidly (De Nijs et al., 2015; Westgate et al., 2022). Their widespread geological occurrence, combined with their highly crushable nature, poses substantial challenges for foundation design and soil-structure interaction analyses (De Nijs et al., 2015; Baldermann et al., 2022; Westgate et al., 2022, 2023, 2024). In offshore applications such as monopiles, sand breakage is critical due to high stress concentrations and cyclic loading, while in nearshore settings it affects embankments, ground improvement, and pile installation through significant grading evolution.

Although glauconite occurs widely in shallow marine deposits, its permissible content in engineering applications remains a critical concern (Westgate et al., 2022). Van Raak (2009) classified glauconite sands as low (<5%), medium (5-40%) and high (>40%) in content with differing engineering mitigation implication. Belgian guidelines (Tedrow, 2002) further restrict glauconite to <5% for construction sand, allowing its use primarily in embankments. Yet laboratory and field observations are inconsistent. Sands containing moderate glauconite contents have, in some cases, exhibited relatively benign behaviour (Ventouras and Coop, 2009; Mentiki et al., 2015), while other studies report marked changes in stress-strain response and deformation characteristics with increasing glauconite content (Konstantinou et al., 2025). Transitions from strain-softening to strain-hardening behaviour have been observed across materials with differing glauconite proportions (Van Raak, 2009; Konstantinou et al., 2025), despite only minor variations in critical-state friction angle. Field evidence from offshore pile installation further suggests that even modest glauconite contents can significantly influence interface behaviour and resistance (Perikleous et al., 2023). These mixed observations suggest that glauconite content influences soil behaviour in complex and non-intuitive ways, and that current empirical guidelines do not fully capture this variability.

Existing studies consistently show that glauconite sands exhibit a high propensity for particle breakage. Laboratory observations (Hossain et al., 2009; Emidio et al., 2009; Westgate et al., 2023; Zou et al., 2025) show that glauconite particles crush more readily than calcareous or carbonate sands, with breakage initiating at relatively low stress levels, e.g., 2 MPa in oedometer tests (Bellotti et al., 1991). This process leads to rapid generation of fines and concurrent changes in particle morphology, which in turn influence key engineering properties including compressibility, strength, and permeability. Breakage-induced changes have been linked to practical issues such as early pile refusal, increased shaft friction, and long-term foundation performance (De Nijs et al., 2015; Westgate et al., 2024). Nevertheless, current understanding remains largely qualitative, and there is a lack of systematic, mineral-specific quantification of how glauconite content governs particle breakage, grading evolution, and macroscopic response. In particular, the coupling between stress, energy dissipation, and particle-scale transformations has not been explicitly established for glauconite-rich systems.

Recent advances in particle-crushing research provide a framework to address these challenges. Arrested-loading tests and high-resolution imaging techniques now allow particle size and shape evolutions to be quantified (Suescun-Florez et al., 2020). Complementary studies on carbonate, silica and coral sands have clarified how stress level, relative density, strain rate, particle shape and coordination number control breakage (Zhang et al., 2016; Zhao et al., 2020; Wu et al., 2020;Yang et al., 2021; Wang et al., 2022; Lei et al., 2024), while energy-based frameworks link macroscopic input work to particle-scale fracture mechanisms (Huang et al., 2017; Xiao et al., 2017, 2019;). More recent theoretical developments further highlight the need to incorporate coevolving grain size and shape descriptors into constitutive models (Buscarnera and Einav, 2021). Although these developments have significantly advanced the understanding of granular breakage, their application to glauconite sands remains limited. Given the distinct mineralogical characteristics and exceptional crushability of glauconite, there is a clear need to extend these frameworks to account for mineral-dependent behaviour.

Motivated by these considerations, this study presents a systematic experimental investigation into the role of glauconite content in governing particle crushing and mechanical response. A series of one-dimensional oedometric compression tests with arrested loading-unloading stages was conducted on pure glauconite, glauconite-silica mixtures, and silica sand. High-resolution measurements of particle size distribution (PSD) and particle shape were performed to quantify grading and morphology evolution.. The objectives were to: (1) characterise the mechanical response and compressibility of sands with varying glauconite contents, and (2) develop quantitative relationships linking stress, energy dissipation, relative breakage, fractal grading evolution, and particle-shape change. By integrating these aspects, this study develops a unified experimental framework that connects particle-scale fragmentation to macroscopic response. These findings enhance the understanding of crushing in glauconitic deposits and support improved offshore foundation design, constitutive modelling, and assessments of pile installation and long-term performance in glauconite-rich sands.

2. Testing materials and methods

2.1. Testing materials

2.1.1 Overview

In this study, two glauconite types with differing maturity levels were selected for its representativeness for the Belgian Continental Shelf while offering logistical access by land. The Paleogene material was sampled from the early Eocene Vlierzele Member (Gentbrugge Formation) at Zwalm, consisting of fine-grained, laminated, green-grey, glauconitic sands deposited in a tidal environment (Kaasschieter, 1961; Houthuys and Gullentops, 1988; Fobe, 1995, 1997; Steurbaut, 2006; Steurbaut et al., 2015). The Neogene material was obtained from boreholes in Tessenderlo, targeting the Tortonian Diest Formation, characterised by bioturbated, cross-bedded glauconitic sands associated with tidal inlet infill systems (Houthuys et al., 2020). These two materials represent distinct geological origins and maturation stages typical of glauconite-bearing sediments in the region.

2.1.2 Sample characterization and preparation

XRD refinement of bulk Vlierzele shows the sample consists of ~18% clays, ~76% quartz, ~5% feldspars and ~1% calcite, while the Diest sample consists of ~30% clays, ~64% quartz, ~5% feldspars and ~1% iron oxides. Sieving in combination with optical incident petrography shows that sand-sized glauconite dominantly has a diameter of 200-300 μm. To properly test the effect of sand-sized glauconite on the mechanical properties of soil, the sand fraction between 100 μm to 500 μm is separated from the rest of the sample by wet sieving.

Glauconite is magnetically separated with a Frantz magnetic separator where strength of the magnet and tilt angle are optimized over several test runs, as shown in Fig. 1 (Adriaens, 2015). This results on the one hand in the 100% glauconite samples and on the other hand the rest fraction consisting dominantly of quartz and ~6-7% feldspars, referred to as "100% silica sand" in this study. The natural glauconite content in the 150µm-1mm fraction is 7.8% and 32.4% for the Vlierzele for Diest samples, respectively.

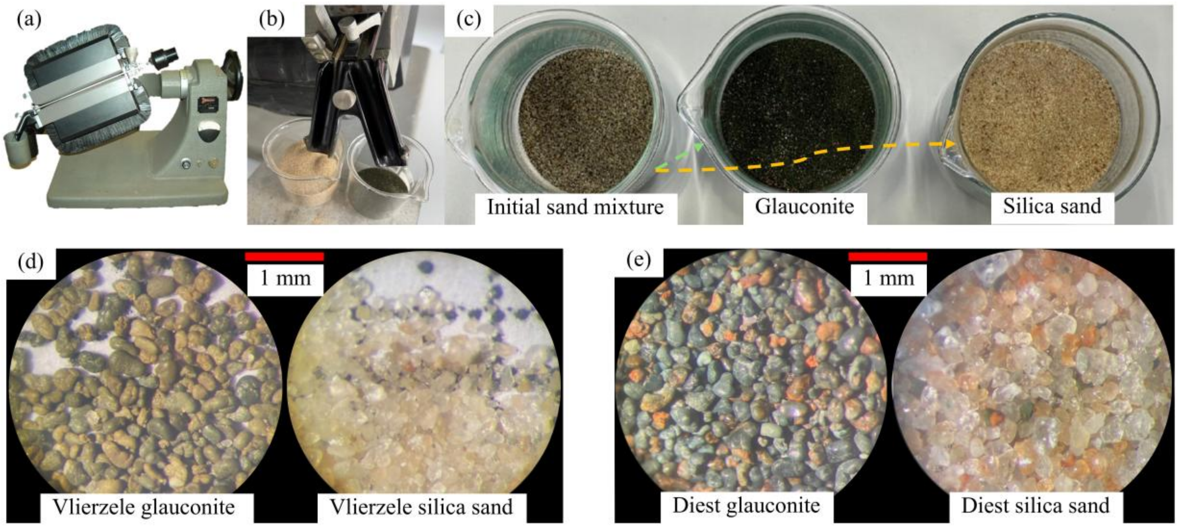

Fig. 1. (a) Frantz magnetic separator; (b) Separated sands at the outlets of the magnetic separator; (c) initial sand mixture alongside separated glauconite and silica sand; (d) photographs of 100% Vlierzele glauconite and silica sand; (e) photos of 100% Diest glauconite and 100% silica sand. Red-coloured particle surfaces indicate oxidation.

Petrographic evaluation of all subsamples and in particular the glauconite, shows relatively mature pelletoidal glauconite grains. While the Vlierzele glauconite is more olive green with yellowish oxidation in color, the Diest glauconite is darker, more turquoise with orange oxidation colors (Fig. 1(e)). Pellets for both sands show the typical maturation "cracks" (Odin and Matter, 2003; López-Quirós et al., 2019; Baldermann et al., 2022). XRD clay mineralogical analyses after Jackson treatment (to purify samples) show the typical mixed layered (ML) nature of the glauconite grains (Fig.A.1). While the Vlierzele sample is dominated by illites over smectites, the Diest sample is dominated by smectite (see Fig.A. 1 (a) and (b) for detailed results). The evolution from dark to light with smectite transitioning to illite, as often considered typical for maturation, is in line with the difference in age of the younger Neogene Diest compared to the older Paleogene Vlierzele glauconite grains. N2-physisorption analyses (Fig.A. 2) show that the Vlierzele glauconite is slightly more porous and has a higher specific surface area compared to the Diest glauconites. More textural parameters of the sand-sized glauconite fractions derived from nitrogen physisorption are listed in Table 1.

Table 1: Textural parameters of the sand-sized glauconite fractions derived from nitrogen physisorption. These were quantified using the Dubinin-Astakhov (DA) theory for micropores (Dubinin and Astakhov, 1971), the Brunauer-Emmett-Teller (BET) theory for specific surface area (Brunauer et al., 1938), the Barrett-Joyner-Halenda (BJH) theory for mesopores (Barrett et al., 1951), and the Gurvich rule for total pore volume (Gurvich, 1915).

	Vlierzele	Diest
Surface Area		
BET Surface Area	87.2304 m²/g	69.6635 m²/g
BJH Adsorption cumulative surface area of pores between 1,7000 nm and 300,0000 nm diameter	50.4340 m²/g	42.7690 m²/g
BJH Desorption cumulative surface area of pores between 1,7000 nm and 300,0000 nm diameter	25.9038 m²/g	23.7887 m²/g
Pore Volume		
Single point adsorption total pore volume of pores less than 275,2179 nm diameter at p/p° = 0,993000000	0.118945 cm³/g	0.087808 cm³/g
Single point desorption total pore volume of pores less than 322,1469 nm diameter at p/p° = 0,994028649	0.119353 cm³/g	0.088216 cm³/g
t-Plot micropore volume	0.005248 cm³/g	0.004278 cm³/g
BJH Adsorption cumulative volume of pores between 1,7000 nm and 300,0000 nm diameter	0.098536 cm³/g	0.072673 cm³/g
BJH Desorption cumulative volume of pores between 1,7000 nm and 300,0000 nm diameter	0.077030 cm³/g	0.055609 cm³/g
Pore Size		
Adsorption average pore diameter (4V/A by BET)	5.4543 nm	5.0418 nm
Desorption average pore diameter (4V/A by BET)	5.4730 nm	5.0653 nm
BJH Adsorption average pore diameter (4V/A)	7.8150 nm	6.7968 nm
BJH Desorption average pore diameter (4V/A)	11.8947 nm	9.3504 nm
Dubinin-Astakhov		
Limiting micropore volume	0.032281 cm³/g	0.025760 cm³/g

2.2. Testing apparatus and testing procedures

2.2.1 Oedometer cell

A stainless steel oedometer cell was designed to systematically investigate the stress-strain behaviour of glauconite and silica sand mixtures under high pressure. The oedometer cell is consist of a top force transmission cap with 19.5 mm diameter loading rod, a thick-walled cylindrical cell, a base with a drainage channel and stainless top/bottom discs for dry tests and porous copper discs for saturated tests (19.8 mm diameter), as illustrated in in Fig. 2 (a) and Fig. 2 (b). The cylindrical cell was designed with an outer diameter of 60 mm, an inner diameter of 20 mm, and a wall thickness of 40 mm, ensuring that the radial deformation under 400 MPa remain negligible (i.e., < 1%, given the Young's modulus of 210 GPa and a Poisson's ratio of 0.26).

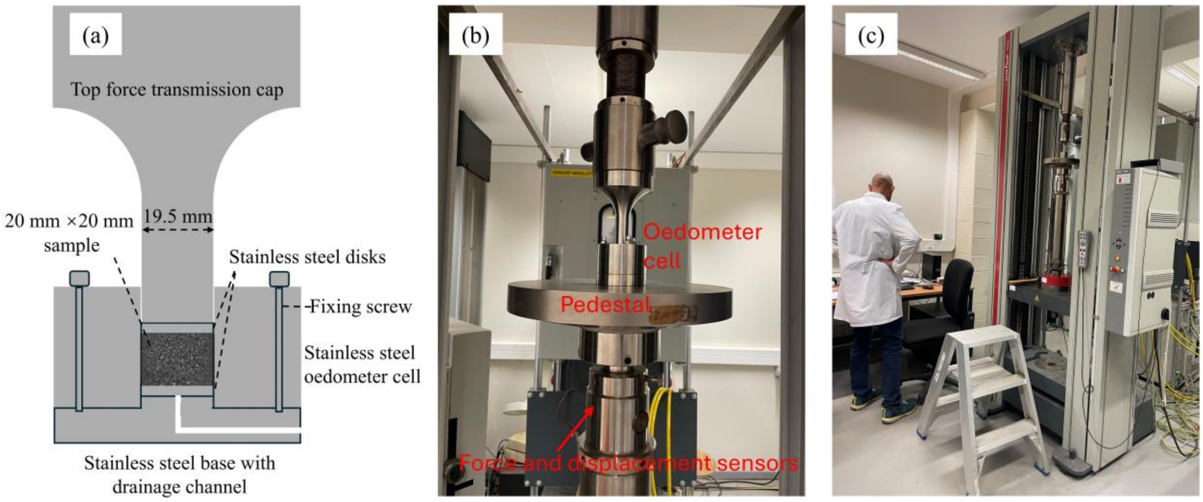

Fig. 2. (a) schematic drawing of the oedometer cell; (b) photograph of the oedometer cell positioned in the loading system; (c) a photo of the overview of the loading system

2.2.2 Loading system

A Zwick Roell Z250 materials testing machine (as shown in Fig. 2 (c)), equipped with a central ball-lead screw, was used to apply and maintain loading and unloading forces on the samples placed in the oedometer cell. The axial displacement was controlled via programmable software, with both force and displacement automatically recorded throughout each test. The machine has a maximum compression force of 250 kN, corresponds to a maximum compressive stress of approximately 2,500 MPa for a sample with a 20 mm diameter.

2.2.3 Particle size and shape quantification system

Conventional sieve and hydrometer methods were unsuitable due to the limited sample quantities, efficiency and accuracy. Laser diffraction provides efficient PSD measurement with small sample volumes but assumes spherical particles, which introduces uncertainty for irregular grains (Eshel et al., 2004). Dynamic imaging, while capable of capturing particle shape, is sensitive to particle orientation (Altuhafi et al., 2013; Wang et al, 2019; Suescun-Florez et al., 2020). To overcome these limitations, a combined laser diffraction and dynamic imaging approach was adopted. The Microtrac SYNC particle size and shape analyser was used to quantitatively determine PSD and morphological parameters. This hybrid technique enables simultaneous measurement of particle size and shape characteristics under identical testing conditions (Grubbs et al., 2021). The system measures particles ranging from 0.3 μm to 2000 μm.

2.3. Testing procedures

2.3.1 Oedometer tests

The arrested loading-unloading technique described by Suescun-Florez et al. (2020) was adopted in this study. This method involves unloading the specimen after reaching a predetermined strain level to determine the unloading modulus and to enable post-test determination of the material’s PSD and morphological parameters.

Prior to sample preparation, the shaft of the top disk, the inner wall of the cylindrical cell and the loading rod were lubricated with a thin layer of silicone grease to minimize friction. A calculated mass of dry material was carefully poured into the oedometer cell using a funnel with a long shaft (approximately 5 cm). The sample was then subjected to vibration for 1-3 minutes to achieve the target height, ensuring a uniform density and void ratio (Suescun-Florez et al., 2020). Stainless steel discs were used for dry tests, and porous copper discs for saturated tests (Fig. 2 (a)).

A preload of 10 N (≈31.8 kPa) was applied prior to each test to ensure full contact between the components and the sample. Loading commenced immediately once the preload force was achieved. A constant displacement rate of 0.1 mm/min was applied during loading and 1 mm/min during unloading.

For tests on dry samples, strain-controlled compression tests were conducted under continuous loading (CL). Each series of tests on the same material was arrested at axial strains ranging from 10% to 40%. For silica sand, the maximum strain was limited to 30% to avoid excessive loading stress that could cause deformation or yielding of the steel loading rod. Once the target strain was achieved, the load was held constant for 1 s, after which unloading commenced.

For tests on saturated samples, after sample preparation, water was added to a level approximately 1 cm above the specimen surface, and the saturation process was maintained for 12 hours before loading. An incremental loading (IL) technique, following ASTM D2435 (2020), was then employed. Specifically, the sample was loaded in six increments until a total axial displacement of at least 6 mm was reached, with each loading step corresponding to a predetermined strain level equivalent to approximately 1 mm of axial displacement (Fig.A. 3).

After each increment, the load was maintained for fixed durations of 1, 2, 4, 4, 4, and 4 hours, respectively, to allow pore water pressure dissipation and ensure that primary consolidation was substantially complete before proceeding to the next increment. The holding duration for each stage was validated as sufficient, as no further axial strain was observed. This stepwise loading process continued until the final target strain was reached, after which the sample was unloaded. For comparison, additional tests using the constant loading rate (CL) technique were conducted on the same material.

In this study, five materials were tested: 100% Diest Glauconite, 100% Vlierzele Glauconite, 32.4% Diest Glauconite mixed with silica sand, 7.8% Vlierzele Glauconite mixed with silica sand, and 100% silica sand. The latter was used as a benchmark for comparing glauconitic sands with typical sand behaviour. A summary of the oedometer tests, including sample type, testing condition, loading mode, and corresponding strain and stress parameters, is presented in Table 2.

Table 2 Summary of oedometer tests in this study.

Test NO.	Test sample (Glauconite content)	Sampling location	Condition	ε_{target}	ε_{max}	Loading rate (mode) (mm/min)	e_0	σ_y (MPa)	σ_{max} (MPa)
1	100% Glauconite	Diest	Dry	10%	11.2%	0.1 (CL)	0.877	5.16	9.83
2	100% Glauconite	Diest	Dry	15%	15%	0.1 (CL)	0.877	5.16	12.13
3	100% Glauconite	Diest	Dry	20%	21.8%	0.1 (CL)	0.895	5.16	24.98
4	100% Glauconite	Diest	Dry	30%	30.4%	0.1 (CL)	0.886	5.16	42.01
5	100% Glauconite	Diest	Dry	40%	40%	0.1 (CL)	0.888	5.16	94.42
6	100% Glauconite	Diest	Saturated	30%	29.8%	0.1 (CL)	0.879	0.45	6.14
7	100% Glauconite	Diest	Saturated	50%	49.4%	0.1 (CL)	0.885	0.45	74.23
8	100% Glauconite	Diest	Saturated	30%	35%	0.1 (IL)	0.877	0.47	7.37
9	100% Glauconite	Diest	Saturated	30%	36%	0.1 (IL)	0.826	0.47	4.57
10	100% Glauconite	Vlierzele	Dry	10%	10.2%	0.1 (CL)	0.902	5.76	9.03
11	100% Glauconite	Vlierzele	Dry	20%	20.3%	0.1 (CL)	0.909	5.76	21.11
12	100% Glauconite	Vlierzele	Dry	30%	30.6%	0.1 (CL)	0.907	5.76	42.33
13	100% Glauconite	Vlierzele	Dry	40%	40.4%	0.1 (CL)	0.911	5.76	84.22
14	32.4% Glauconite	Diest	Dry	10%	10.0%	0.1 (CL)	0.876	6.62	15.92
15	32.4% Glauconite	Diest	Dry	20%	19.7%	0.1 (CL)	0.887	6.62	35.16
16	32.4% Glauconite	Diest	Dry	30%	29.4%	0.1 (CL)	0.874	6.62	81.72
17	32.4% Glauconite	Diest	Dry	40%	39.8%	0.1 (CL)	0.888	6.62	222.93
18	7.8% Glauconite	Vlierzele	Dry	10%	9.9%	0.1 (CL)	0.903	10.78	21.44
19	7.8% Glauconite	Vlierzele	Dry	20%	19.6%	0.1 (CL)	0.896	10.78	47.58
20	7.8% Glauconite	Vlierzele	Dry	30%	29.3%	0.1 (CL)	0.897	10.78	106.04

21	7.8% Glauconite	Vlierzele	Dry	40%	36.3%	0.1 (CL)	0.897	10.78	222.94
22	7.8% Glauconite	Vlierzele	Dry	40%	38.3%	0.1 (CL)	0.901	10.78	260.58
23	100% silica sand	Diest	Dry	10%	10.1%	0.1 (CL)	0.863	14.95	27.27
24	100% silica sand	Diest	Dry	20%	20.0%	0.1 (CL)	0.880	14.95	61.98
25	100% silica sand	Diest	Dry	30%	30.02%	0.1 (CL)	0.867	14.95	165.49
26	100% silica sand	Diest	Saturated	30%	35.3%	0.1 (IL)	0.863	14.85	157.66

Note: ε_{max} denotes the maximum axial strain; CL denotes continuous loading with a constant loading rate; IL denotes incremental loading

2.3.2 Particle size and shape analysis

After each arrested test, the entire material was collected and prepared for particle size and shape analyses. Glauconite samples subjected to higher strain levels (particularly at 40% axial strain) exhibited a slightly greater degree of particle bonding. These agglomerates were gently separated by light finger rubbing and soft brushing, a procedure shown to introduce negligible additional breakage due to the low applied stresses relative to particle strength (Suescun-Florez et al., 2020).

Subsamples, typically containing thousands to tens of thousands of particles (depending on particle size), were analysed using a Microtrac SYNC particle size and shape analyser. Particle size and shape were analysed simultaneously using the integrated laser diffraction and dynamic imaging modules. The laser diffraction module provided volume-based PSD and equivalent spherical diameters (e.g., D_{10}, D_{50}, D_{100}) , while the imaging module captured 2D projections of individual particles. Image processing yielded key geometric parameters, perimeter (P), projected area (A), and Feret dimensions (FLength and FWidth), from which shape descriptors such as aspect ratio, sphericity, roundness, and circularity were derived (Fig. 3 (b)-(c)). All measurements were performed on large particle populations and averaged to ensure statistical robustness. The combined use of diffraction and imaging provides a consistent characterisation of both particle size and morphology.

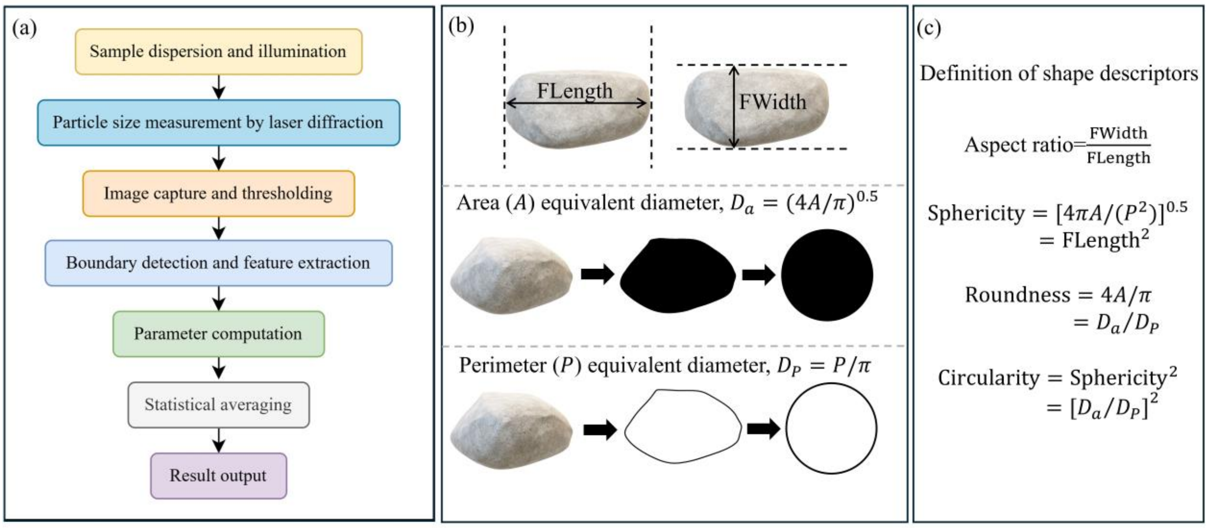

Fig. 3. (a) Workflow of the Microtrac SYNC particle size and shape analyser integrating laser diffraction and dynamic image analysis; (b) Illustration of geometric parameters used to define the area (A), perimeter (P), Feret Length (FLength) and Feret Width (FWidth); (c) Definitions of shape descriptors, including aspect ratio, sphericity, roundness, and circularity.

3. Results

3.1. Mechanical behaviour of glauconitic and silica sands

3.1.1 Repeatability

Although individual tests on samples with the same glauconite content were subjected to loading and unloading at different axial strain levels, the resulting stress-strain responses and compression planes (Figs. 4-7)) exhibit consistent patterns and reasonable reproducibility. The minor scatter observed among tests can be attributed to small variations in initial boundary conditions (e.g., void ratio and seating stress) (Suescun-Florez et al., 2020) and the inherent heterogeneity of the soil, highlighting the inherent difficulty of achieving perfectly identical specimen states and boundary conditions during sample preparation.

3.1.2 Stress-strain response and compression characteristics

This section presents the stress-strain response and compression characteristics obtained from the oedometer tests. Mechanical behaviour is illustrated through the stress-strain relationship (axial stress, σ, versus axial strain, ε) and the corresponding compression plane, where the specific volume, $v = 1 + e$, is plotted against σ on a semi-logarithmic scale. The yield point is defined as the point of maximum curvature on the compression plane (McDowell and Humphreys, 2002; Nihaaj et al., 2025). From this point, the yielding stress σ_y, axial strain at yielding ε_y, and specific volume at yielding v_y are determined, as shown in Fig. 4-7 and Figs. 9-10. The post-yield slope, λ, represents the local gradient of elastic-plastic volumetric strain, and the unloading slope, κ, corresponds to the local gradient of elastic volumetric strain, both obtained by linear fitting (McDowell et al., 1996). The threshold plastic work per unit volume when particle crushing commences in one-dimensional compression is calculated as (Huang et al., 2014; Xiao et al., 2019): $W_{th} = \int_0^{\varepsilon_y} \sigma d\varepsilon$.

Fig. 4 (a) compares the stress-strain response of 100% Diest glauconite and 100% Vlierzele glauconite. Despite differences in mineral composition, both materials exhibit broadly similar mechanical behaviour, with nearly overlapping stress-strain curves up to about 30% strain, indicating comparable stiffness and compressibility. Beyond 30% strain, the Diest glauconite develops slightly higher strength than the Vlierzele glauconite, which may be attributed to its slightly coarser mean particle size or denser packing fabric, promoting more efficient stress transmission and greater resistance to particle rearrangement under large compressive strains. All curves display pronounced strain hardening beyond ~20% strain, consistent with progressive particle crushing and rearrangement. This is consistent with the mechanisms reported by Suescun-Florez et al. (2020) for silica and coral sands tested under similar 1D compression conditions.

The corresponding compression curves (Fig. 4 (b)) show a clear bilinear trend in semi-log space, indicating a distinct yielding transition. During the initial loading stage, the specific volume decreases slowly and almost linearly with increasing stress, suggesting an elastic compression regime dominated by particle rearrangement without significant breakage. Once the yield stress is exceeded, the specific volume decreases more rapidly, indicating the onset of particle crushing and progressive fabric densification. Linear fittings to the pre- and post-yield portions of the curves yield transition stresses of approximately 5.16 MPa for Diest glauconite and 5.76 MPa for Vlierzele glauconite. The corresponding work input at yielding is 0.149 MJ/m^3 and 0.184 MJ/m^3 for Diest and Vlierzele glauconite, respectively. Overall, , both materials exhibit similar compressibility, with only minor differences in post-yield behaviour.

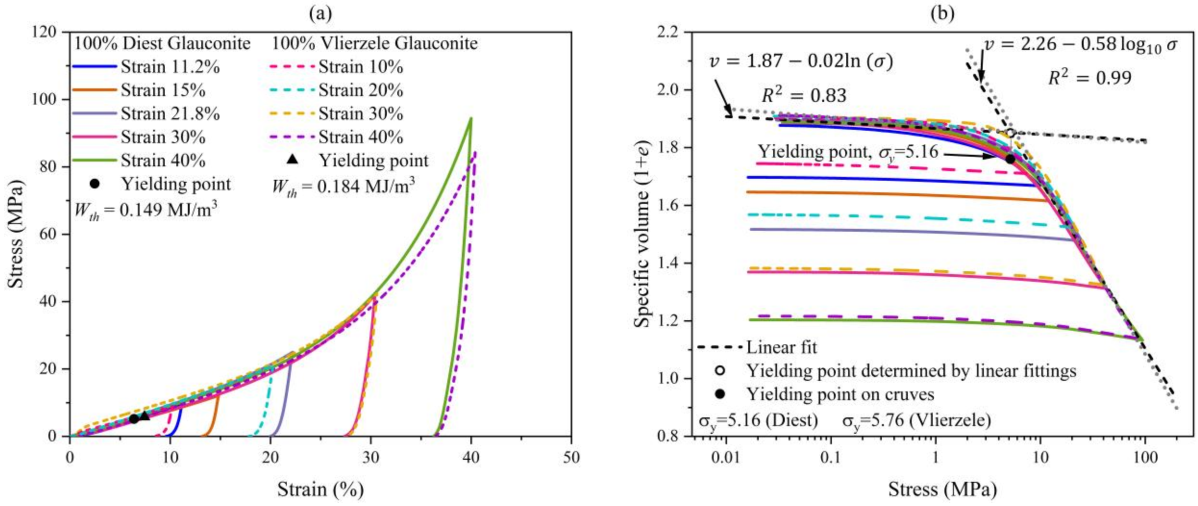

Fig. 4. Comparison between 100% Diest glauconite and 100% Vlierzele glauconite: (a) stress-strain; (b) compression plane.

Fig. 5 and Fig**.** 6 present the stress-strain and specific volume-stress relationships for the naturally formed Diest and Vlierzele samples, containing 32.4% and 7.8% of glauconite, respectively. The overall trends are consistent with those observed for the pure glauconite materials shown in Fig. 4. Both mixtures exhibit a continuous strain-hardening response up to yielding, followed by further strength increase until unloading at the predefined strain levels. Again, the stress-strain curves show concave-up trajectories beyond approximately 20% strain, indicating progressive particle crushing and fabric densification. The corresponding specific volume-stress plots display well-defined bilinear trends in semi-log space, marking distinct yield points. Limited volumetric change is observed before yielding, followed by rapid compression once particle crushing becomes dominant. The yielding stress increases with decreasing glauconite content, from 6.6 MPa in the natural Diest sample to 10.8 MPa in the natural Vlierzele sample, reflecting the greater load-bearing contribution of the silica grains. Despite the higher yield stress and energy input at yielding in the natural Vlierzele sample (W_{th}=0.289 MJ/m^3) compared with the Diest mixture (W_{th}=0.163 MJ/m^3), both materials display broadly similar compressibility and deformation behaviour, indicating that glauconite content primarily governs the yielding characteristics of these naturally formed sands.

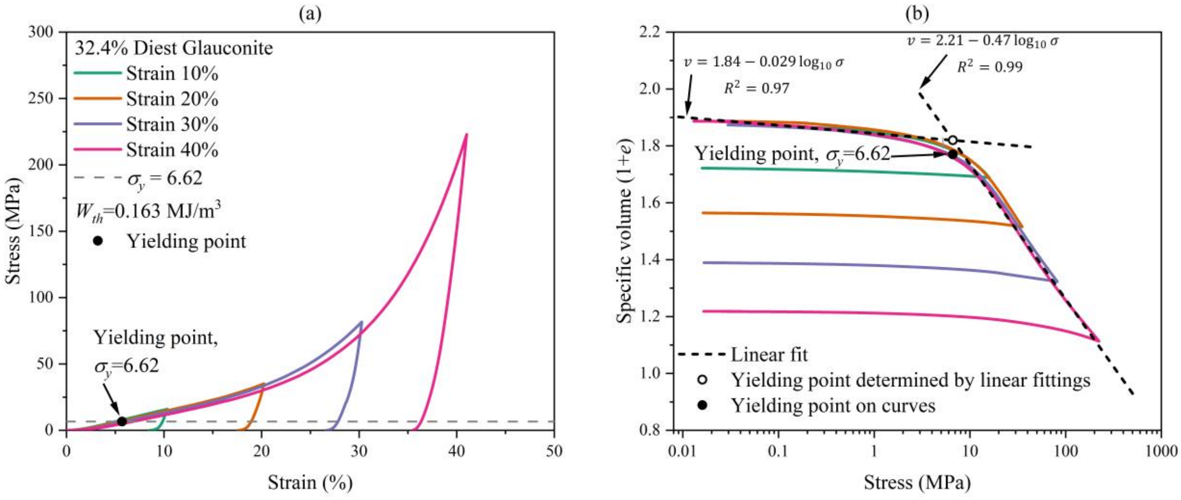

Fig. 5. Naturally formed Diest sample, 32.4% glauconite with 67.6% silica sand: (a) stress-strain; (b) compression plane.

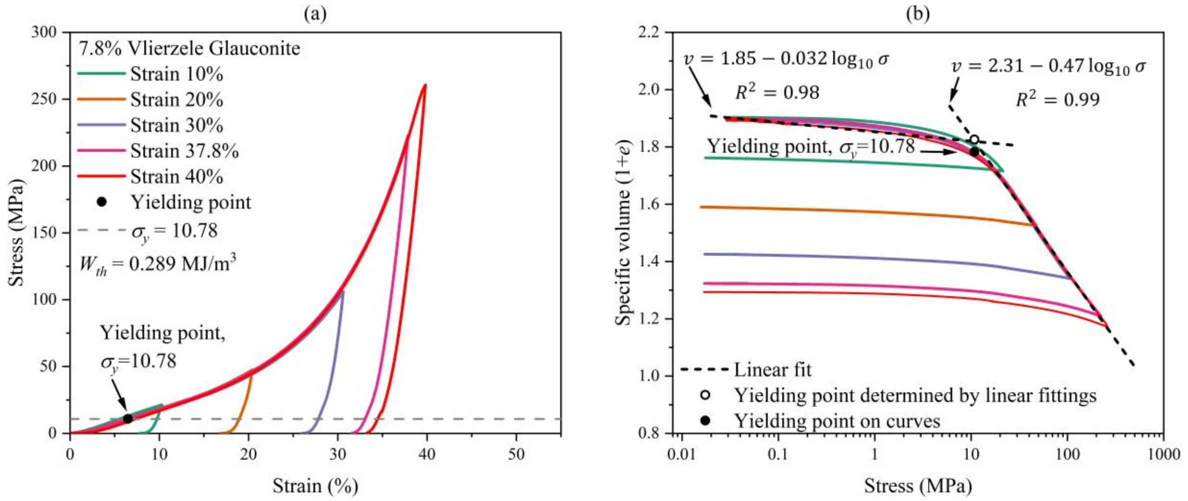

Fig. 6. Naturally formed Vlierzele sample, 7.8% glauconite with 92.2% silica sand: (a) Stress-strain; (b) compression plane.

Fig. 7 presents the stress-strain and specific volume–stress relationships for the 100% silica sand sample under uniaxial oedometric compression, together with stress–strain curves for silica sand and coral sand from Florez et al. (2020) for comparison. In Fig. 7 (a), the measured stress-strain response is broadly consistent with previous data reported by Florez et al. (2020) for pure silica sand, although the stress levels observed here are slightly lower than those of their silica sand tests. Fig. 7 (b) shows the corresponding specific volume-stress relationship, which follows a bilinear trend in semi-logarithmic space. The high yield stress, σ_y=14.95 MPa, confirm the strong mechanical strength of silica sand compared with the glauconitic samples. This value falls within the range reported for dry silica sand under 1D compression (σ_y=14-22 MPa) by Nakata et al. (2010). The corresponding work input at yielding (W_{th}=0.319 MJ/m^3) is also notably higher than those of the glauconitic materials (Figs. 4-6), reflecting the greater stiffness and crushing resistance of silica grains.

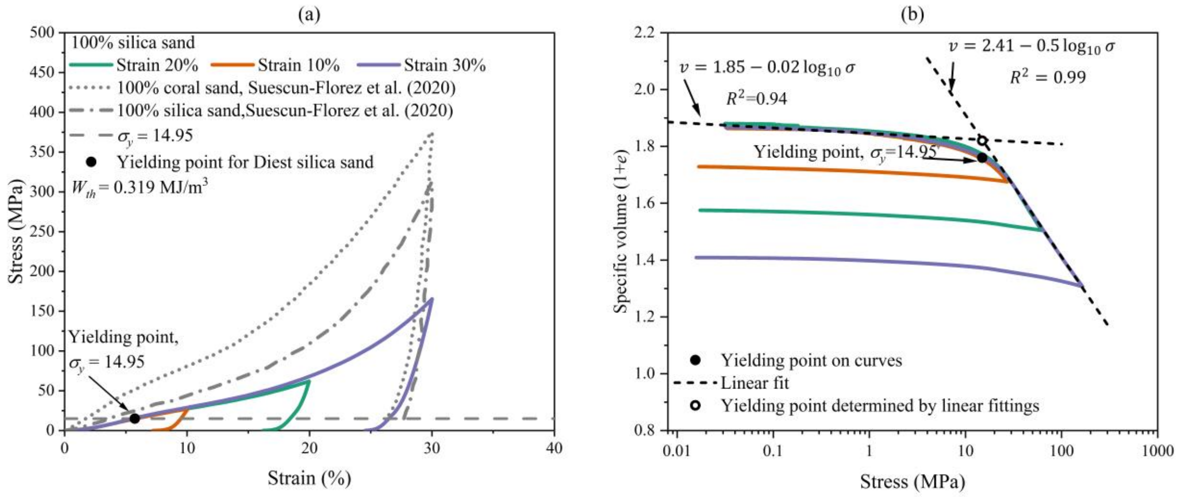

Fig. 7. 100% silica sand: (a) Stress-strain; (b) compression plane.

3.1.3 Influence of glauconite content

Fig. 8 illustrates the influence of glauconite content on the stress-strain responses of glauconite-silica sand mixtures arrested at 30% strain. As glauconite content decreases, both stiffness and strength increase, with silica-rich samples exhibiting steeper strain-hardening and higher stresses (Fig. 8 (a)). The corresponding specific volume-stress relationships (Fig. 8 (b)) display consistent bilinear behaviour, indicating clear yielding transitions. While initial specific volumes vary slightly, post-yield curves shift to higher stress levels with increasing silica content. Data from Emidio et al. (2009) for 100% glauconite are also shown for comparison but do not clearly capture yielding due to limited stress levels. Fig. 8 (c) quantifies the dependence of yielding stress (σ_y) and work input at yielding (W_{th}) on glauconite and silica contents. Both parameters increase nonlinearly with silica proportion (or decrease with glauconite content), following power-law relationships (R^2>0.92). These results confirm that mechanical strength and energy absorption capacity are strongly controlled by glauconite content, with silica-dominated mixtures exhibiting higher stiffness and particle crushing resistance.

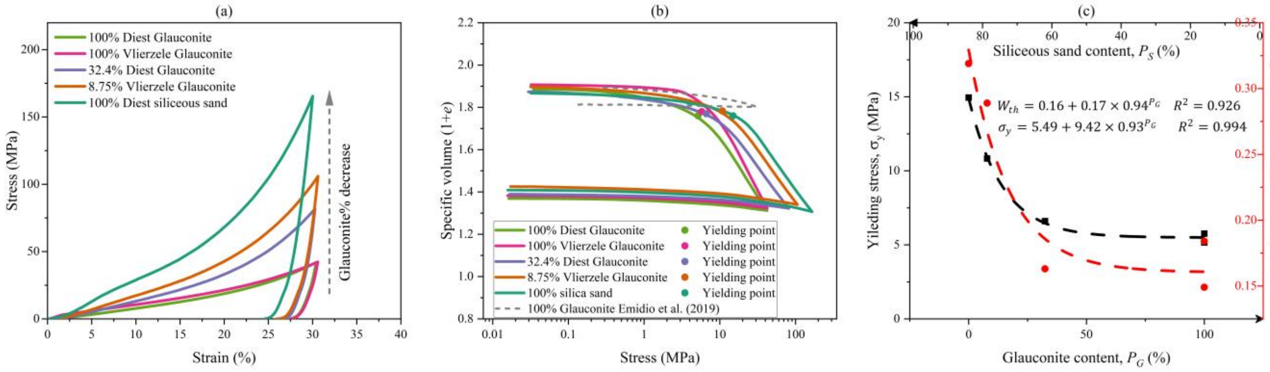

Fig. 8. Influence of glauconite content: (a) stress-strain response up to 30% strain; (b) compression plane; (c) yielding stress and as functions of glauconite/silica content.

3.1.4 Effects of water and loading pattern

Fig. 9 illustrates the effect of water saturation and loading pattern on the mechanical response of 100% Diest glauconite under 1D compression. Fig. 9 (a) compares the stress-strain behaviour under dry and saturated conditions, using both continuous loading (CL) and incremental loading (IL) modes. The dry sample with CL (Test 5) exhibits the highest stiffness and strength, reaching a yield stress of 5.16 MPa and a peak stress of 94.2 MPa at 40% of strain. In contrast, the saturated samples (Tests 6, 7,8 and 9) show substantially reduced strength, regardless of loading pattern, with yielding stresses of approximately 0.45-0.47 MPa and significantly lower energy input at yielding (W_{th}=0.012-0.013 MJ/m³). The IL tests (Tests 8 and 9) display stepwise strain responses due to load-hold cycles, yet their overall mechanical trends are consistent with the CL results at tested strains. At 40% strain, the stress of Test 6 (16.96 MPa) is much lower than that of the dry Test 5, despite both being conducted under CL, indicating that water saturation significantly weakens glauconite. Fig. 9 (b) presents the corresponding specific volume-stress relationships. All curves exhibit the characteristic bilinear trend, with a sharp reduction in specific volume after yielding. The saturated samples show much higher compressibility and lower post-yield stiffness compared with the dry condition. These results demonstrate that water saturation markedly weakens the glauconite structure due to clay mineral (smectite) swelling, reducing its yield stress and energy absorption capacity, while the loading pattern (CL vs IL) exerts a secondary influence on the overall mechanical response.

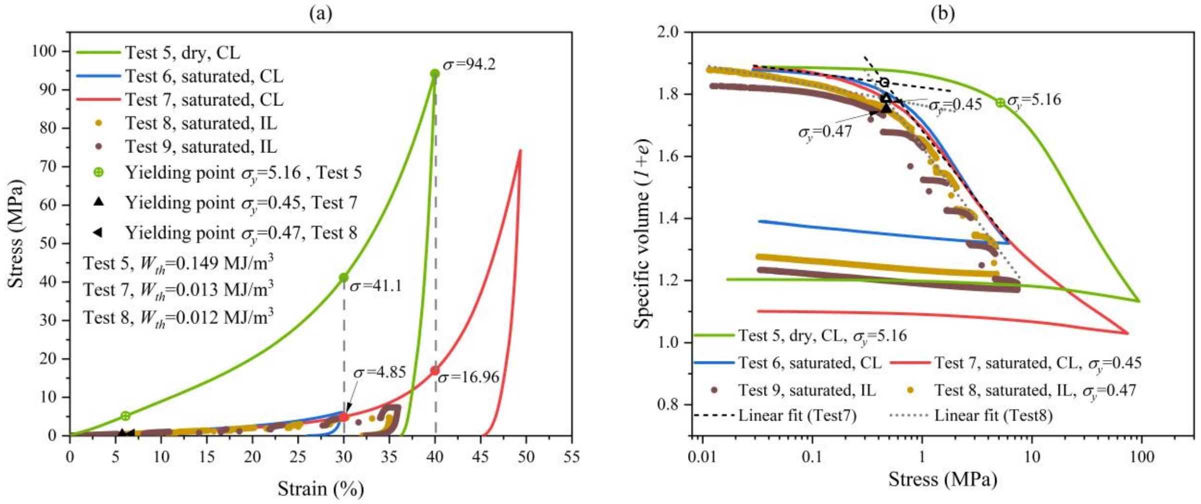

Fig. 9. Effect of water saturation and loading pattern on 100% glauconite sand: (a) stress-strain; (b) compression plane.

Fig. 10 illustrates the effect of water saturation on the mechanical behaviour of 100% silica sand under 1D compression. Fig. 10 (a) compares the stress-strain responses of the dry (Test 25, CL) and saturated (Test 26, IL) samples. Both show similar yielding stresses (σ_y≈14.5-14.95 MPa), but the dry specimen exhibits higher stiffness and strength, reaching a peak stress of 165.6 MPa at 30% of strain, while the saturated sample attains only 107 MPa. Fig. 10 (b) presents the corresponding specific volume-stress relationships, both exhibiting bilinear trends with distinct yield points and similar post-yield slopes of -0.50 and -0.51, respectively. A comparison between Fig. 9 and Fig. 10 shows that water saturation reduces the stress of 100% silica at 30% strain by 35.3%, whereas the reduction for 100% Diest glauconite reaches 88.2%, highlighting the markedly higher water sensitivity of glauconitic material due to the presence of clay minerals, particularly smectite.

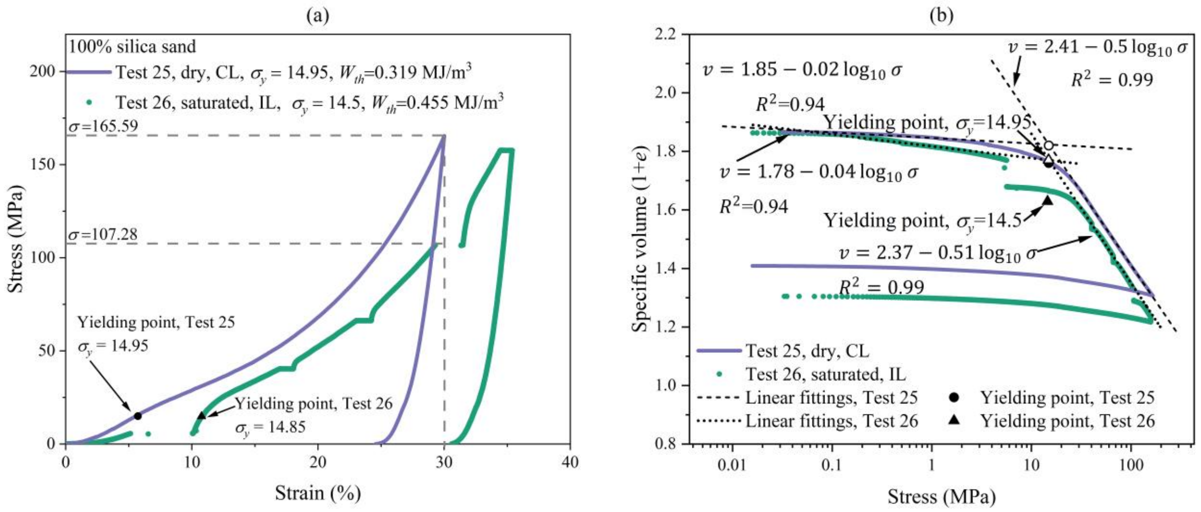

Fig. 10. Effect of water on 100% silica sand: (a) stress-strain; (b) compression plane.

These results align with previous studies showing that water weakens soil strength under oedometric compression (Miura and Toyotoshi, 1975; Ham et al., 2010; Wils and Haegeman, 2014). This effect has been attributed to water accelerating particle crushing and enhancing compressibility by reducing surface energy and weakening particle asperities. The pronounced strength loss and increased compressibility observed in saturated glauconite are therefore consistent with the general weakening trend reported for other crushable soils, although the underlying mechanisms require further investigation. In contrast, Cavarretta et al. (2010) reported negligible water effects in ballotini glass beads, attributed to their strong silica composition and smooth, non-porous surfaces. This contrast indicates that the influence of water on particle breakage is highly mineral-dependent, being significant for weak, micro-porous and clayey materials, particularly those containing swelling clays (e.g., smectites), such as glauconite but relatively minor for dense, silica-rich materials.

3.2. Microscopic and particle-scale observation of the crushing process

Fig. 11 shows stereomicroscope photographs illustrating the progressive crushing of 100% Diest glauconite, 32.4%

Diest glauconite, and 100% silica sand arrested at different strain levels. All three materials exhibit a similar progression of particle breakage, evolving from minor surface abrasion at 10-20% strain to pronounced fragmentation beyond 30%, consistent with the observations of Suescun-Florez et al. (2020) for silica sand and Xiao et al. (2019) for carbonate sand. However, the extent of breakage at 30% strain differs among materials: the 32.4% Diest glauconite and 100% silica sand samples show more severe crushing and finer debris formation, whereas the 100% Diest glauconite largely retain original morphology but with significant surface abrasion. These observations suggest that while the overall breakage mechanism is similar, the degree of particle damage depends on mineral composition and grain strength. For all materials, very few particles appear to have survived undamaged at largest strain level, indicating that the maximum particle size may decrease. This observation contrasts with Suescun-Florez et al. (2020), who reported that a few larger silica grains remained intact at 30% strain, likely due to their more angular morphology.

Fig. 12 shows representative 2D particle projections at d_{90}, d_{50} and d_{10} for 100% Diest Glauconite and 100% silica sand. Both materials display progressive particle size reduction with increasing strain, reflecting continuous crushing and fines generation. Larger particles (d_{90}) remain relatively intact up to 20% strain but become noticeably smaller and more irregular beyond 30%. Finer fractions (d_{50} and d_{10}) show rapid fragmentation, indicating preferential breakage of smaller grains (Coop et al., 2004; Russell and Muir Wood, 2009; McDowell and De Bono, 2013). Silica sand shows a slightly greater degree of size reduction than glauconite at 30% strain, consistent with its higher brittleness and the greater stresses reached during compression.

Fig. 13 presents the microscopic evidence of particle breakage mechanisms in saturated 100% Diest Glauconite (Test 8). The vertical slice extracted from the mid-plane of the specimen (Fig. Fig. 13 (a) and (b)) for polarized-light micrographs. Localized micrographs (Fig. 13 (c)) reveal three dominant modes of particle breakage (as schematically illustrated in Fig. 13 (d)): (i) abrasion/chopping, characterized by surface polishing and edge chopping (red dashed ellipses); (ii) splitting, manifested as splitting failures of elongated particles along weak planes (blue dashed ellipses); and (iii) crushing/comminution, marked by extensive internal cracking and grain pulverization (green dashed ellipses). These mechanisms coexist and reflect the combined influence of particle strength and local force transmission, consistent with established observations in granular materials (Nakata et al., 2001; Einav, 2007a; Zhao et al., 2020; Wang et al., 2026).

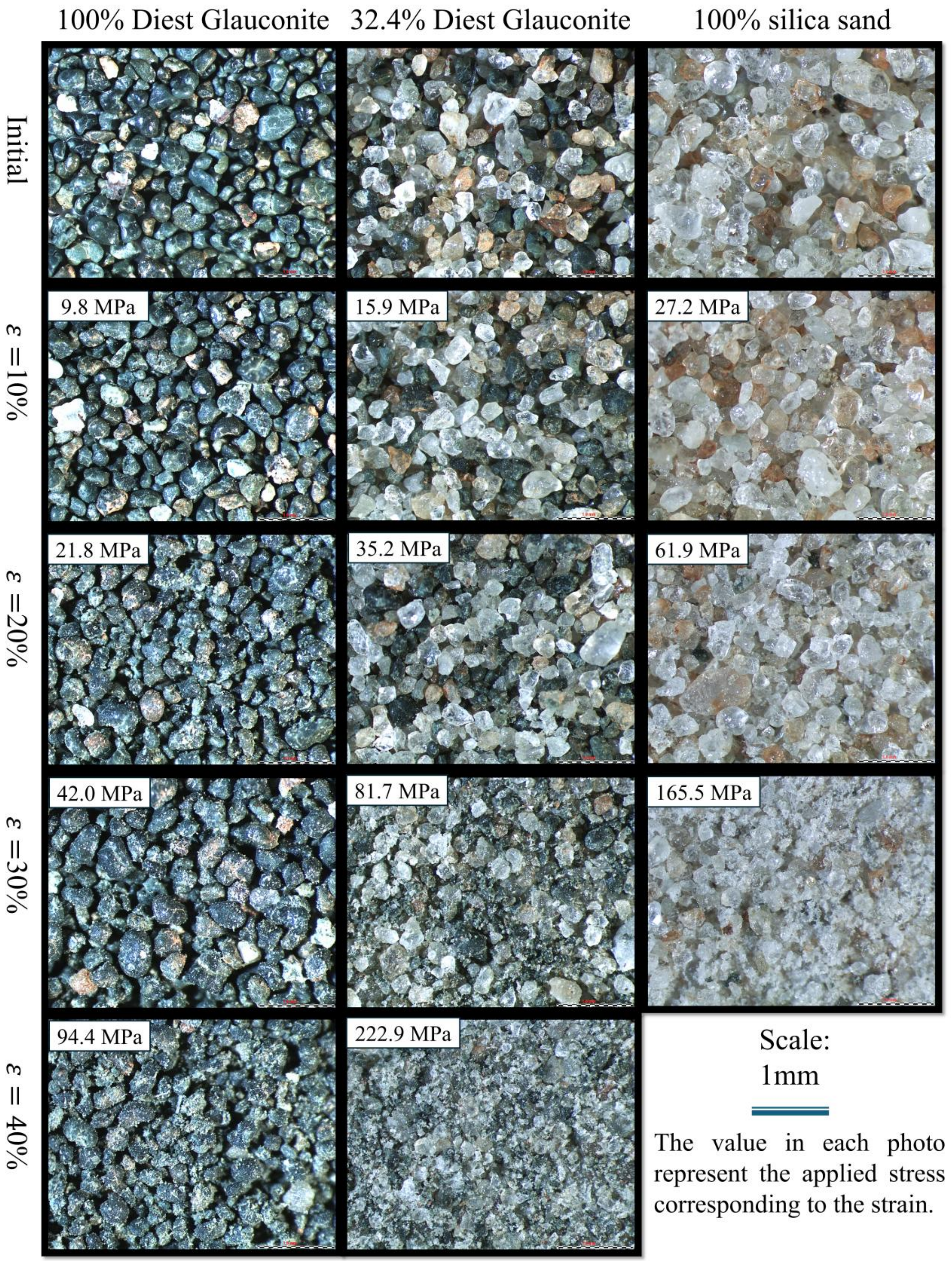

Fig. 11. Stereomicroscope photographs illustrating the progressive crushing of 100% Diest Glauconite, 32.4% Diest Glauconite, and100% Diest silica sand arrested at different strain levels.

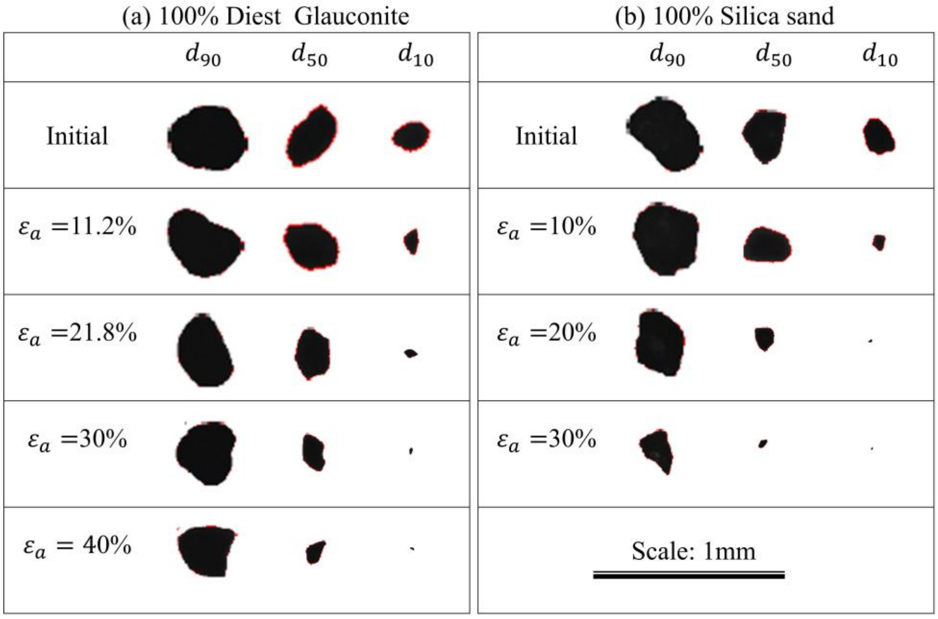

Fig. 12. Representative particle shapes at d_{90}, d_{50} and d_{10} with increasing axial strain for (a) 100% Diest Glauconite and (b) 100% silica sand.

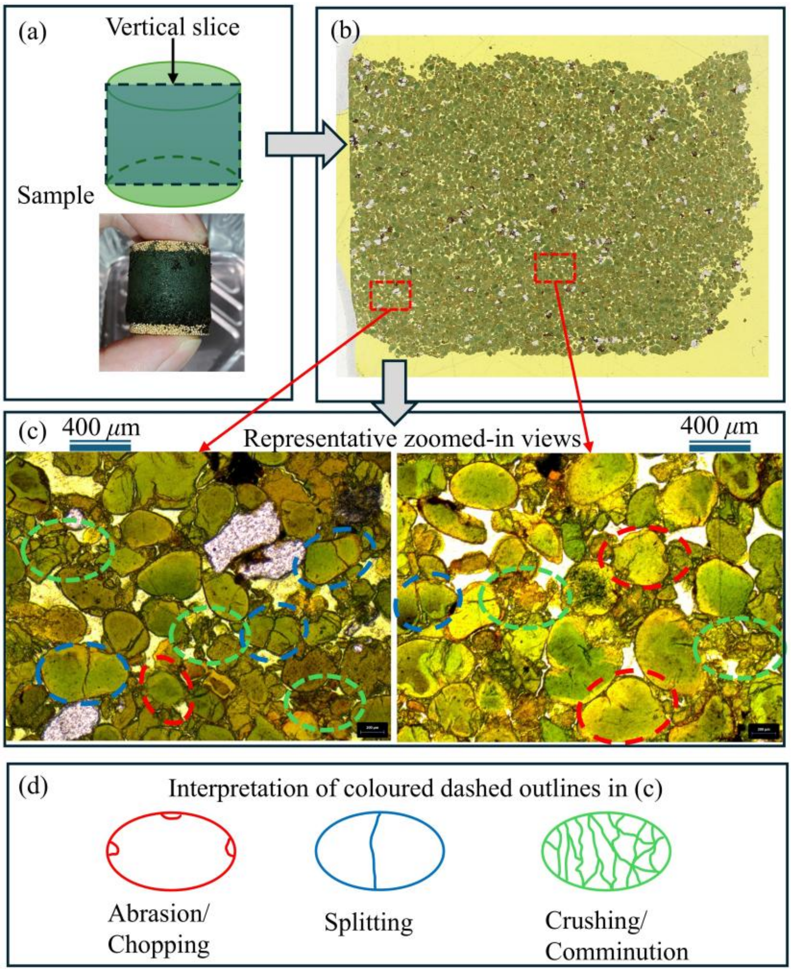

Fig. 13. Microstructural observations of glauconite grains after uniaxial compression. (a) Cylindrical specimen and schematic of the vertical slice used for microscopy. (b) Cross-sectional micrograph of the polished slice. (c) Polarized-light micrographs showing typical grain-scale damage: abrasion, splitting, and crushing. (d) Schematic illustration of the three dominant breakage modes: abrasion/chopping (red), splitting (blue), and crushing/comminution (green).

3.3. Quantitative analysis of particle size evolution

This section presents the PSDs obtained from 1D compression tests on dry glauconite-silica mixtures arrested at different strain levels. Grading evolution is quantified using the relative breakage index (Einav, 2007b), which measures the shift of the PSD relative to reference states and enables direct comparison with other grading state parameters, such as breakage index (Hardin, 1985), the grading state index (Muir Wood, 2007) and modified grading state index (Li et al., 2026). Another parameter, the fractal dimension of PSD, is also introduced and will be explained in Section 3.3.2.

Fig. 14 illustrates the definition of the index of relative breakage B_r proposed by Einav (2007b):

$$B_r = \frac{B_t}{B_p} = \frac{\mathrm{Area}(ACDG)}{\mathrm{Area}(ACEF)} \tag{1}$$

where B_t is the total breakage, defined as the area between the initial PSD and the current PSD $\mathrm{Area}(ACDG)$, and B_p is the breakage potential, defined as the area between the initial PSD and ultimate fractal PSD $\mathrm{Area}(ACEF)$. The ultimate fractal PSD curve can be expressed as (Li et al., 2026):

$$P_m(d < d_s) = 100\left(\frac{d_s^{3-D_{su}} - d_{sumin}^{3-D_{su}}}{d_{sumax}^{3-D_{su}} - d_{sumin}^{3-D_{su}}}\right) \tag{2}$$

where d is the particle size, d_s is the particle size corresponding to a given point on the PSD curve, and D_{su}, d_{sumin} and d_{sumax} denote the fractal dimension, and the minimum and maximum particle size of the ultimate fractal PSD, respectively. The concept of the relative breakage is essentially the same as the grading state index proposed by Muir Wood (2007) and the modified grading state index (Li et al., 2026).

If the current PSD follows a fractal distribution, it can be expressed as:

$$P_m(d < d_s) = 100\left(\frac{d_s^{3-D_s} - d_{scmin}^{3-D_s}}{d_{scmax}^{3-D_{su}} - d_{scmin}^{3-D_{su}}}\right) \tag{3}$$

where D_s, d_{scmin} and d_{scmax} denote the fractal dimension, and the minimum and maximum particle size of the current fractal PSD, respectively.

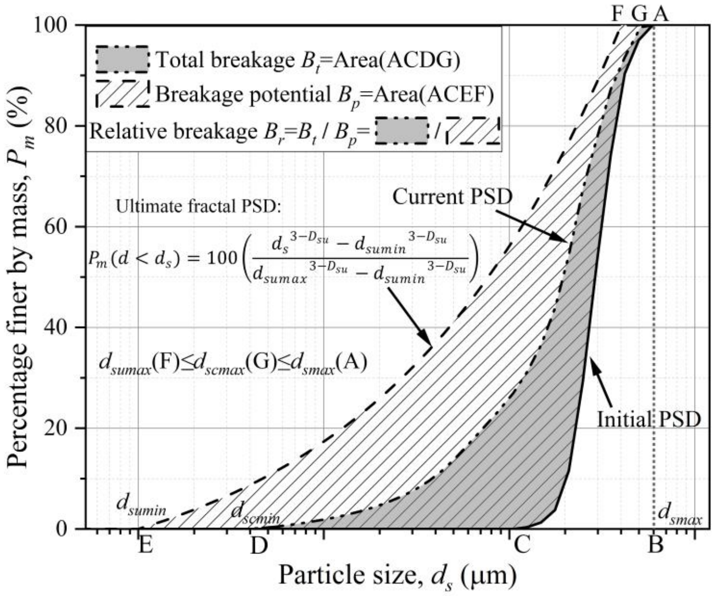

Fig. 14. Definition of relative breakage (Einav, 2007b).

3.3.1 Evolution of particle size distribution and relative breakage

Fig. 15 shows the evolution of PSDs and corresponding relative breakage (B_r) for dry glauconite-silica mixtures arrested at different axial strains. In Fig. 15 (a)-(e), all samples exhibit a systematic shift of the PSD curves toward finer sizes with increasing strain, indicating continuous particle breakage. It can be noted that both the maximum and minimum particle sizes evolve with strain, consistent with previous observations (Wils and Haegeman, 2014; Manso et al., 2018; Suescun-Florez et al., 2020; Jiang et al., 2026). Specifically, the minimum particle size of 100% glauconite decreases to approximately 1 μm, while that of the glauconite-silica mixtures and 100% silica sand reaches about 0.5 μm. The most significant reduction in maximum particle size is observed in 100% silica sand, from 497 μm to 296 μm.

Some studies, however, have reported that the maximum particle size remains largely unchanged during crushing, as larger grains generally possess more contact points and higher coordination numbers, resulting in lower average contact forces and, consequently, reduced breakage probability (McDowell and Bolton, 1998; Ciantia and O'Sullivan, 2020). Accordingly, several researchers have reported that the maximum particle size remains effectively constant when calculating relative breakage (Huang et al., 2014; Xiao et al., 2017). In contrast, the results in this study suggest that even the coarser silica grains underwent noticeable size reduction, likely due to the high applied stress levels (Wils and Haegeman, 2014; Manso et al., 2018; Suescun-Florez et al., 2020). Therefore, it is reasonable to assume that $d_{sumax} \leq d_{scmax} \leq d_{smax}$, where d_{smax} denotes the maximum particle size of the initial PSD, as illustrate in Fig. 14.

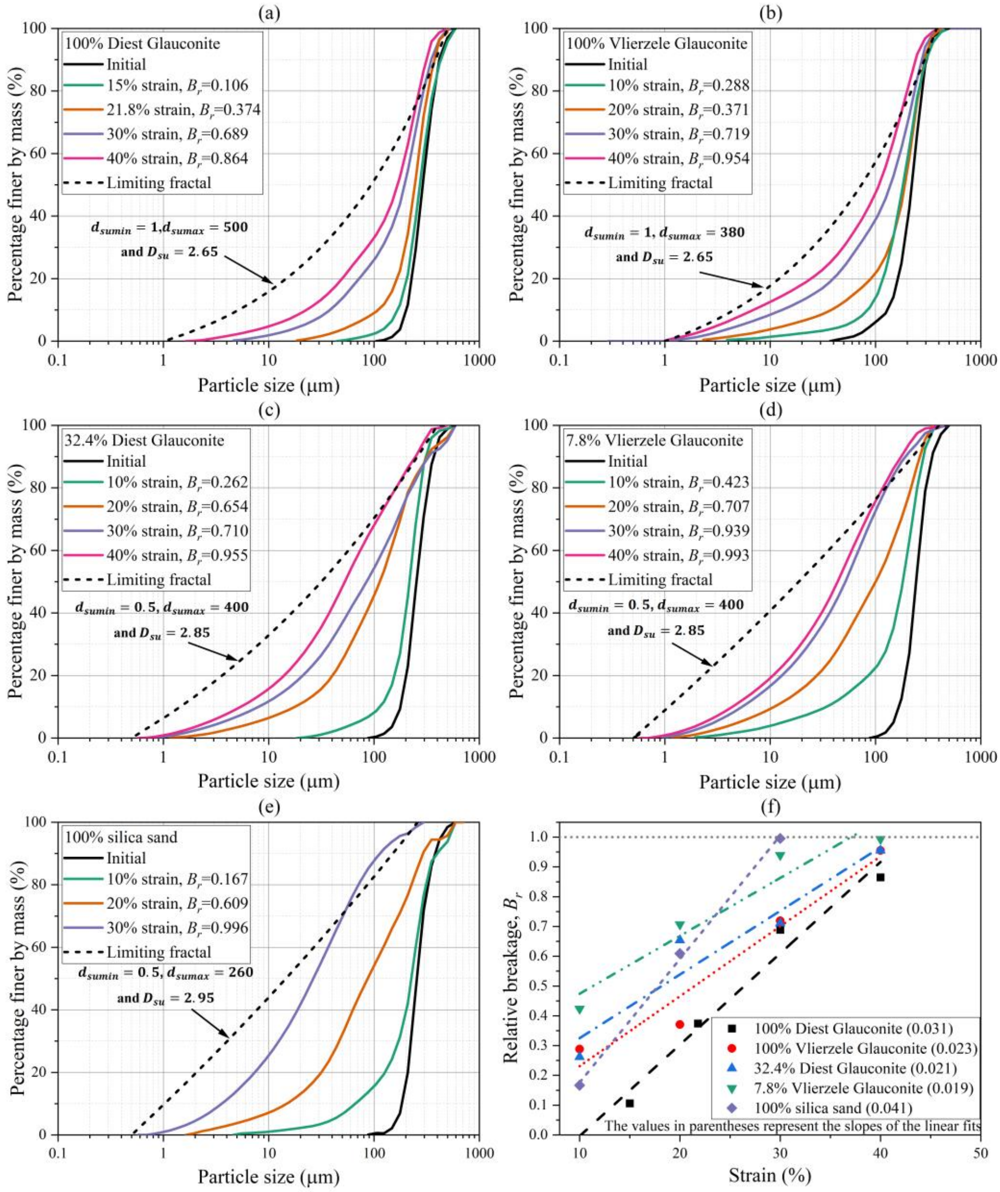

Fig. 15. Evolution of PSD and the relative breakage. (a) 100% Diest glauconite; (b) 100% Vlierzele glauconite; (c) 32.4% Diest glauconite; (d) 7.8% Vlierzele glauconite; (e) 100% silica sand; (f) relative breakage plotted against strain.

For most soils formed by fragmentation or crushing processes, the ultimate fractal dimension D_{su} typically ranges between 2.30 and 2.95 (Perfect, 1997; McDowell and Bolton, 1998; Coop et al., 2004; Russell, 2010; Huang et al., 2017; Li et al., 2022; Tong et al., 2026). However, soils produced by other geological mechanisms may exhibit D_{su} values outside this range. For example, Storti et al. (2003) reported that the fractal dimension of fault gouge increases from 1.8 to 3.6 as the sampling area approaches the shear band. In this study, the value of ultimate fractal dimension is inferred based on two considerations: (i) it should not be smaller than the maximum fractal dimension measured experimentally, and (ii) it should remain consistent with the observed trend of progressive particle crushing. The values of d_{sumin} and d_{sumax} were taken from the minimum and maximum measured values, respectively. Accordingly, the assumed D_{su} values satisfy the above criteria. All values and the corresponding calculated B_r are listed in the Fig. 15 (a)-(e).

Fig. 15 (f) shows the relationship between B_r and axial strain. B_r increases linearly with strain, consistent with the observations of Yu (2017) and Wu et al. (2020) on silica sands, with steeper slopes indicating greater breakage rates. Among the samples, 100% silica sand exhibits the greatest breakage rate (B_r/ε).

3.3.2 Evolution of fractal dimension

Many studies have shown that PSD of granular materials progressively evolves toward a fractal form during particle crushing, with fractal dimension increasing as crushing progresses (McDowell et al., 1996; Russell, 2011; Xiao et al., 2016; Huang et al., 2017; Yao et al., 2023). As shown in Fig. 16 (a), the PSDs of 100% Diest Glauconite at different axial strains become progressively finer and linear in log-log space, reflecting the development of a fractal distribution. Particle sizes larger than the effective particle size (d_{10}) were used in linear fitting, thus the fractal dimension was determined based on the 'full' PSD to account for the evolution of both maximum and minimum particle sizes. The slopes of the fitted lines ($3 - D_s$) yield fractal dimensions that increase from D_s=0.289 at ε=15% to D_s=2.178 at ε =40%.

Fig. 16 (b) presents the variation of D_s with strain. The data were fitted using an asymptotic function, as shown in the figure. All materials exhibit a rapid initial increase in fractal dimension that gradually approaches an upper limit D_{su}, corresponding to the ultimate fractal state. The fitted parameters (shown in parentheses) demonstrate excellent correlation (R^2>0.9) for all cases. Overall, the results confirm that particle crushing drives the PSD toward a stable fractal form, with both the rate of evolution and the ultimate fractal dimension dependent on mineral type and initial grading.

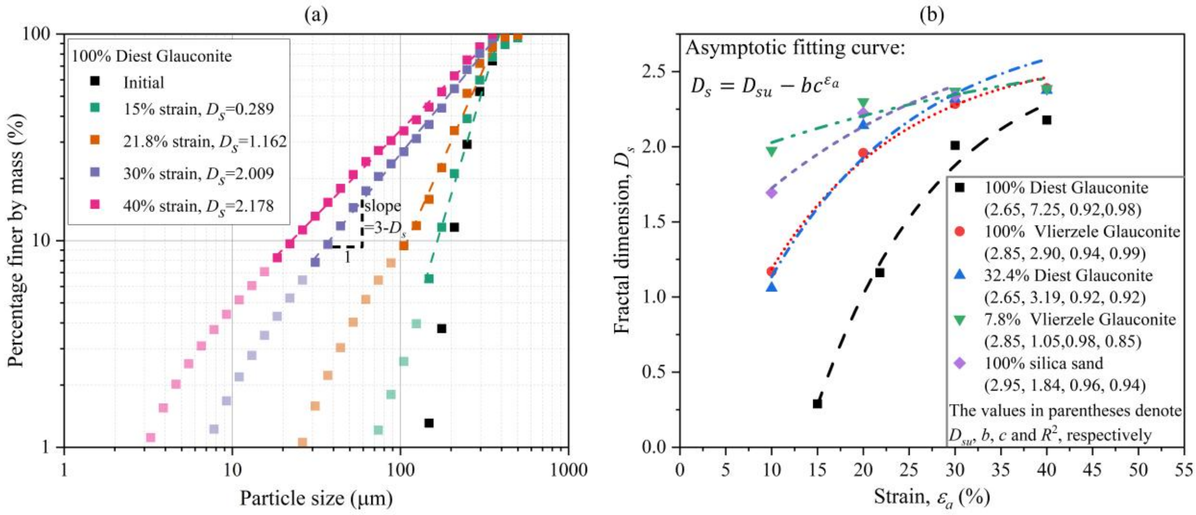

Fig. 16. (a) Example of determining the fractal dimension D_s; (b) evolution of fractal dimension with strain.

Fig. 17 shows the relationship between B_r and D_s for different glauconite-silica mixtures. In all cases, B_r increases nonlinearly with D_s, following an exponential trend expressed as:

$$B_r = ne^{(D_s/m)}+\beta \tag{4}$$

where n, m, and β are fitting parameters. The fitted curves exhibit high coefficients of determination (R^2>0.85). Huang et al. (2017) reported a linear the relationship between B_r and D_s for quartz sand. This difference reflects material-dependent breakage behaviour. Quartz tends to crush progressively and proportionally, whereas glauconite-rich mixtures undergo more abrupt fragmentation once breakage initiates. The exponential form therefore captures the accelerated increase in fractal dimension associated with the rapid fragmentation of these weaker minerals.

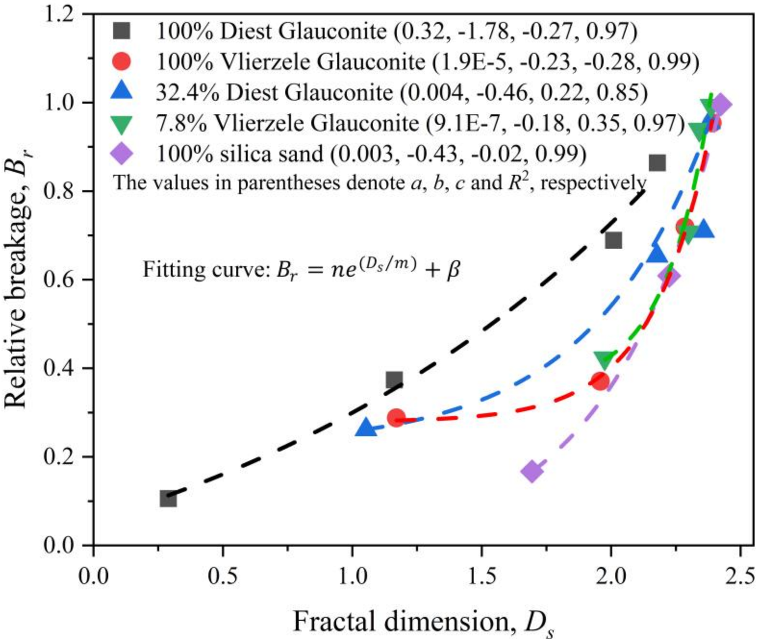

Fig. 17. Relationship between relative breakage and fractal dimension

3.4. Relationships between energy dissipation, stress, relative breakage and fractal dimension

To integrate the two key factors influencing particle breakage, i.e., stress and strain, the concept of specific plastic work is adopted to evaluate the energy dissipation during the particle breakage process. The specific plastic work done per unit volume can be calculated as follows (Huang et al., 2014; Xiao et al., 2019):

$$W = W_{th} + \int_{\varepsilon_y}^{\varepsilon} \sigma \mathrm{d}\varepsilon \tag{5}$$

where σ and ε are the axial stress and strain, respectively, and ε_y is the axial strain at yielding. $W_{th} = \int_0^{\varepsilon_y} \sigma d\varepsilon$ represents the threshold plastic work per unit volume when particle crushing commences in 1D compression test. The values of W_{th} for each test are presented in Figs. 4-7 and Fig. 9.

Fig. 18 (a) presents the relationship between specific work and stress for 1D compression tests on dry samples containing different amounts of glauconite. Linear regression yields an R^2 value of 0.991 for the reported tests. Fig. 18 (b) shows the relationship between relative breakage and stress. Huang et al. (2014) proposed a theoretical relationship between stress and relative breakage, given as:

$$B_r = \omega \ln\left(\frac{\sigma}{\sigma_y}\right) \tag{6}$$

where ω is a fitting coefficient. Equation (6) was applied to each set of experimental data, resulting in an average R^2 value of 0.860. Alternative fitting forms, such as the logistic model, have also been used by other researchers (Li et al., 2022).

Fig. 18 (c) presents the relationship between relative breakage and specific work. The relationship between B_r and W proposed by Huang et al. (2014) can be expressed as:

$$B_r = \xi \ln\left(1 + \frac{W - W_{th}}{W_0}\right) \tag{7}$$

where $W_0 = \sigma_y \Lambda(-v_y^{-1})$ represents the characteristic plastic work dissipated in the particle breakage process, v_y is the specific volume at yielding and $\Lambda = \lambda - \kappa$, ξ is a material constant. When Equation (7) was applied to each dataset in Fig. 18 (c), low R^2 values were obtained. Fitting all experimental data together yields an R^2 value of 0.879. However, this formulation may yield $B_r > 1$, as shown in Fig. 18 (c), which is mathematically inconsistent with the definition of relative breakage. To overcome this limitation, an alternative relationship was developed:

$$B_r = 1 - e^{\left(-\xi \ln\left(\frac{W+a}{W_{th}}\right)\right)} \tag{8}$$

Or equivalently,

$$B_r = 1 - \left(\frac{W_{th}}{W+a}\right)^{\xi} \tag{9}$$

where a is a fitting parameter. The logarithmic term $\alpha \ln\left(\frac{W+a}{W_{th}}\right)$ is derived from Equation (6) by substituting stress with specific work, since a linear relationship between stress and specific work was observed (as reported in Fig.

18 (a)). The best fit of Equation (9) (R^2=0.901) gives:

$$B_r = 1 - \left(\frac{32.59}{33.03+W}\right)^{7.58} \tag{10}$$

In this expression, B_r asymptotically approaches 1 as W increases. This form effectively captures the nonlinear growth behaviour associated with energy dissipation and particle breakage observed in this study.

Fig. 18 (d) shows the relationship between fractal dimension D_s and specific work W for tests on dry samples with varying glauconite content. The results show that D_s increases rapidly with increasing W at low specific work levels, followed by a gradual approach to an asymptotic value (ultimate fractal dimension D_{su}) as W continue to increase. The data are represented by an exponential function:

$$D_s = 3(1 - e^{-0.42W}) \tag{11}$$

This indicates that the fractal dimension tends to stabilize near 3 at very high specific work levels, suggesting that particle fragmentation becomes progressively limited once most crushable grains have failed and additional energy is dissipated primarily through bond formation or surface rearrangement. The consistent trend across samples with varying glauconite contents implies that the evolution of PSD with increasing energy input follows a similar fractal pattern, largely independent of glauconite proportion and glauconite type considered in this study.

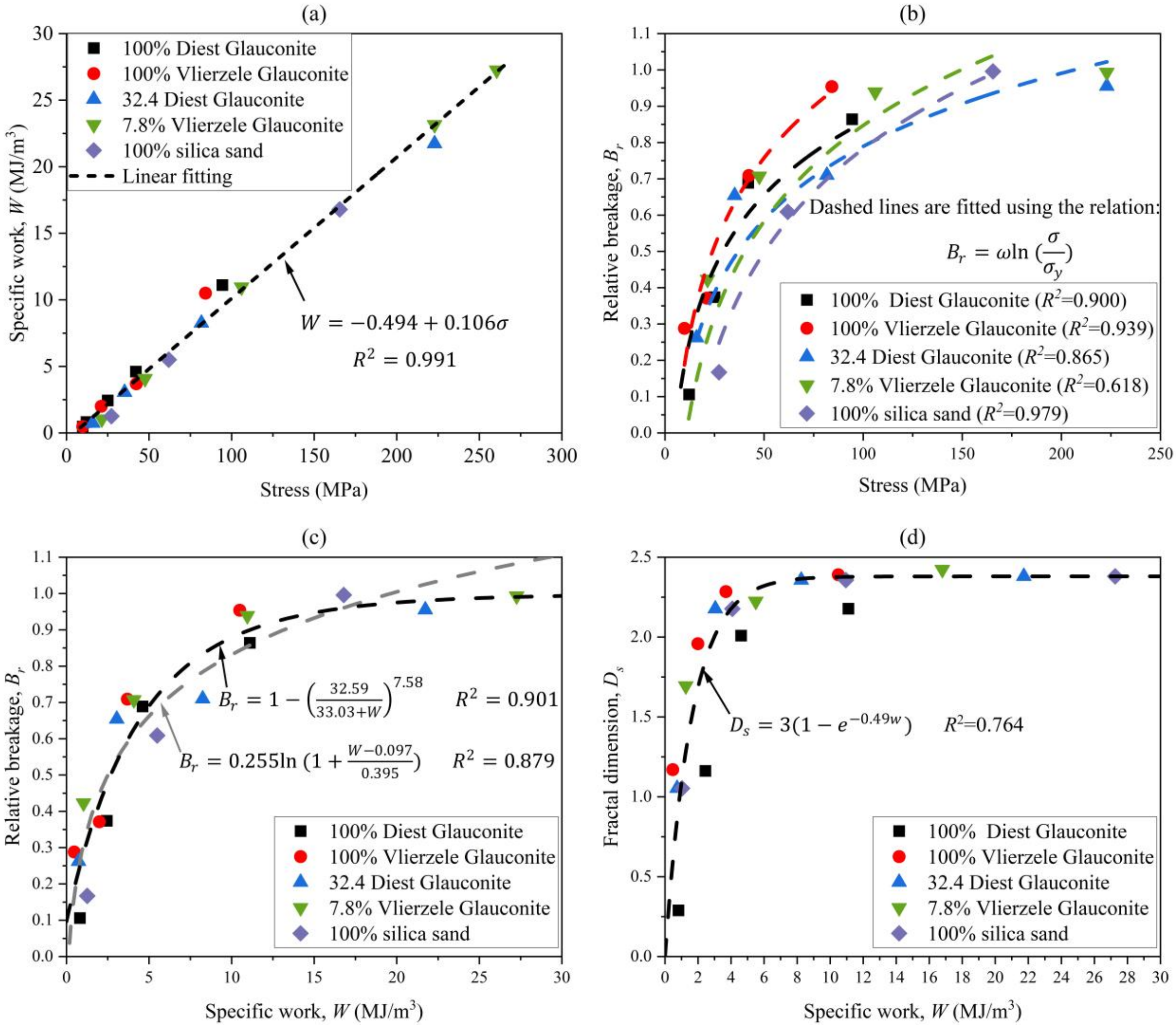

Fig. 18. (a) Specific work plotted against stress; (b) relative breakage plotted against stress; (c) relative breakage plotted against specific work; (d) fractal dimension plotted against specific work.

3.5. Particle shape evolution

The evolution of particle shape descriptors (i.e., aspect ratio, sphericity, roundness and circularity) with increasing relative breakage is shown in Fig. 19. The values of each shape descriptor were obtained by averaging measurements from thousands to tens thousands of individual particles. To describe the evolution of mean aspect ratio α with relative breakage B_r, the theoretical relationship proposed by Buscarnera and Einav (2021) is aslo considered here. They introduced a mathematical expression that links between particle breakage to shape evolution through aspect ratio:

$$\alpha = \alpha_L + (\alpha_0 - \alpha_L)e^{-C_\alpha(B/(1-B))} \tag{12}$$

where B is a breakage internal variable, which is a particular form of the relative breakage B_r (Einav, 2007b); α_0 is the aspect ratio prior to breakage; C_α is a constant controlling the rate of shape evolution in relation with the breakage growth rate; and α_L is the ultimate value of α.

Fig. 19 (a) shows the relationships between the aspect ratio α and the relative breakage B_r for samples with varying glauconite contents under dry testing condition. In all cases, the α decreases with increasing B_r, indicating progressive particle elongation. The relationship is well captured by Equation (12), with excellent agreement (R^2 ranging from 0.937 to 0.991). The initial aspect ratio α_0 and the ultimate aspect ratio α_L vary slightly among the samples, reflecting differences in initial particle morphology and resistance to shape change. Samples containing glauconite generally exhibit higher α_L than silica sand, suggesting a greater tendency to retain equant shapes during breakage.

Fig. 19 (b)-(f) show the evolution of shape descriptors, i.e., aspect ratio, mean sphericity, roundness, and circularity, with increasing B_r. Aspect ratio and roundness decrease by 3.4-8.4% and 4.0-9.3%, respectively, indicating increasing elongation and irregularity. Sphericity (0.8-1.8%) and circularity (0.9-3.6%) shown only minor reductions, suggesting that breakage primarily modifies particle elongation rather than overall smoothness of the particle outline. Overall, glauconitic samples generally exhibit higher aspect ratio and sphericity than silica sand, consistent with their more equant morphology during crushing.

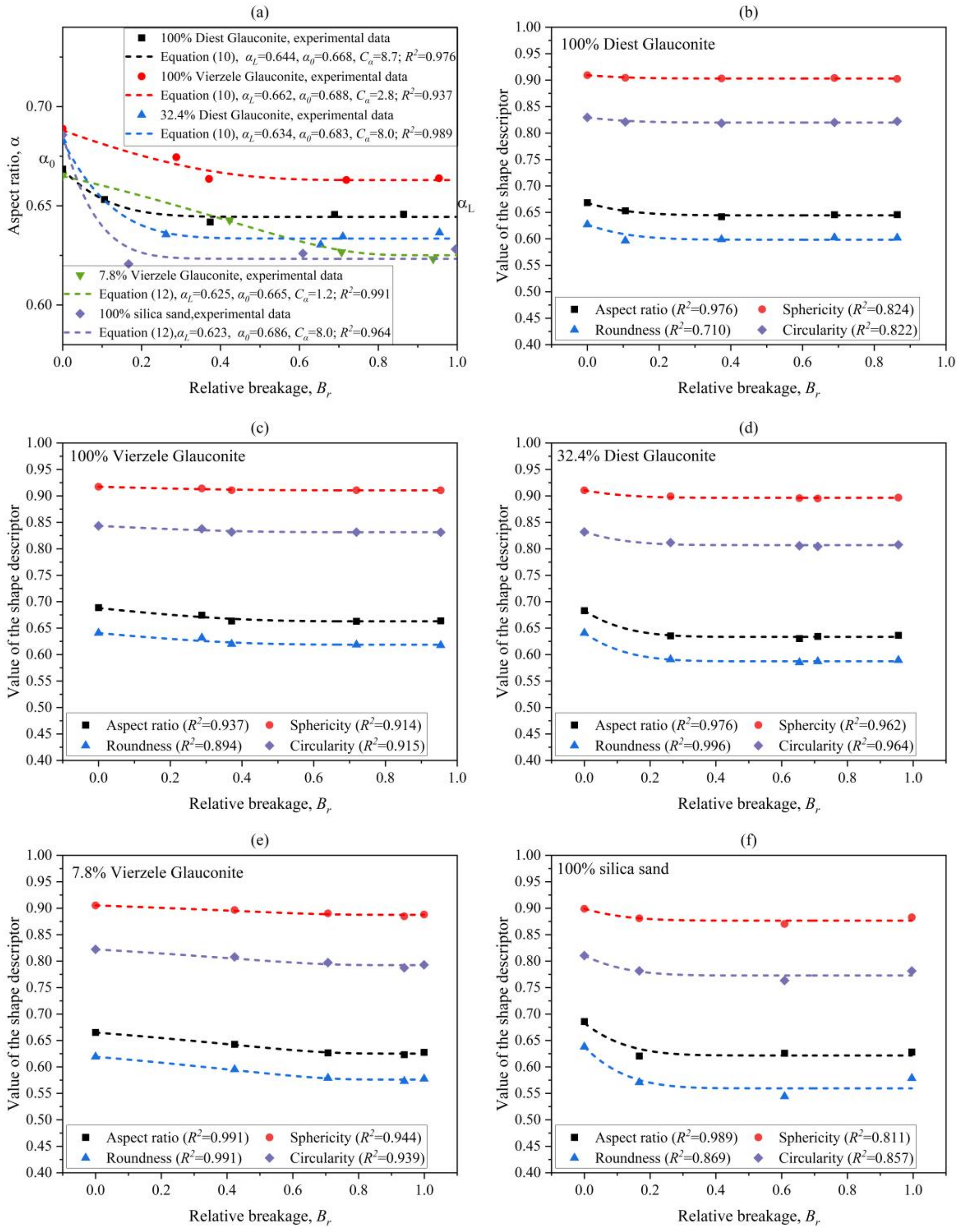

Fig. 19. (a) Relationship between mean aspect ratio and relative breakage for the tested samples; (b-f) Variations of shape descriptors with relative breakage for (b) 100% Diest Glauconite, (c) 100% Vlierzele Glauconite, (d) 32.4% Diest Glauconite, (e) 7.8% Vlierzele Glauconite, and (f) 100% silica sand.

Equation (12) was further applied to fit the evolution of these shape descriptors, showing excellent agreement with the experimental data (R^2=0.71-0.99). These results confirm that Equation (12) can be extended and effectively capture the observed trends in particle shape evolution. A modified form of Equation (12) can be expressed as:

$$s = s_L + (s_0 - s_L)e^{-C_\alpha(B_r/(1-B_r))} \tag{13}$$

where s represent a shape descriptor (i.e., aspect ratio, sphericity, roundness, or circularity), s_0 is the initial value and s_L is an ultimate value.

The relative frequency distributions of aspect ratio, sphericity, roundness, and circularity for the 100% Diest Glauconite and 100% silica sand at different breakage levels are shown in Fig. 20. All descriptors exhibit unimodal distributions, indicating consistent overall shape populations during breakage.

For 100% Diest Glauconite (Fig. 20 (a)), the most significant change in aspect ratio occurs between the initial state and the first breakage level (B_r=0.106), characterized by a reduction in the proportion of nearly equant particles ($\alpha \geqslant 0.775$) and a corresponding increase in elongated particles ($\alpha \leqslant 0.725$). With further breakage (B_r=0.374-0.864), the distributions remain almost unchanged, indicating that most shape modification occurs during the earliest phase of crushing. This observation is consistent with the trend shown in Fig. 19 (a). The initial mean aspect ratio, α_0=0.668, and the ultimate mean aspect ratio, α_L=0.644 are indicated in the plot, highlighting a slight but systematic tendency toward elongation. Similar reduction in aspect ratio in 1D compression has been observed for calcareous sands by Wei et al. (2022). Consistently, sphericity and circularity show minimal variation, with values concentrated at high levels (≈0.85-0.95), while roundness exhibit a noticeable increase in frequency within the 0.5-0.6 range and a decrease in 0.625-0.8, indicating particle edges become slightly more irregular due to abrasion and crushing (as illustrated in Fig. 13). These results confirm that although glauconite particles undergo breakage, their shapes become slightly more elongated and their edges slightly sharper, their overall outlines and smoothness are largely preserved.

In contrast, the silica sand exhibits more pronounced shape evolution. The aspect ratio distributions shifts markedly after initial breakage (B_r=0.167), with increased frequency of elongated particles and reduced equant particles. Similar trends are observed for sphericity, roundness, and circularity, which all shift towards lower values, indicating increased elongation, angularity, and irregularity. These changes are consistent with brittle fracture of quartz grains. As with glauconite, subsequent breakage leads to only minor additional changes, suggesting that most shape modification occurs during early fragmentation.

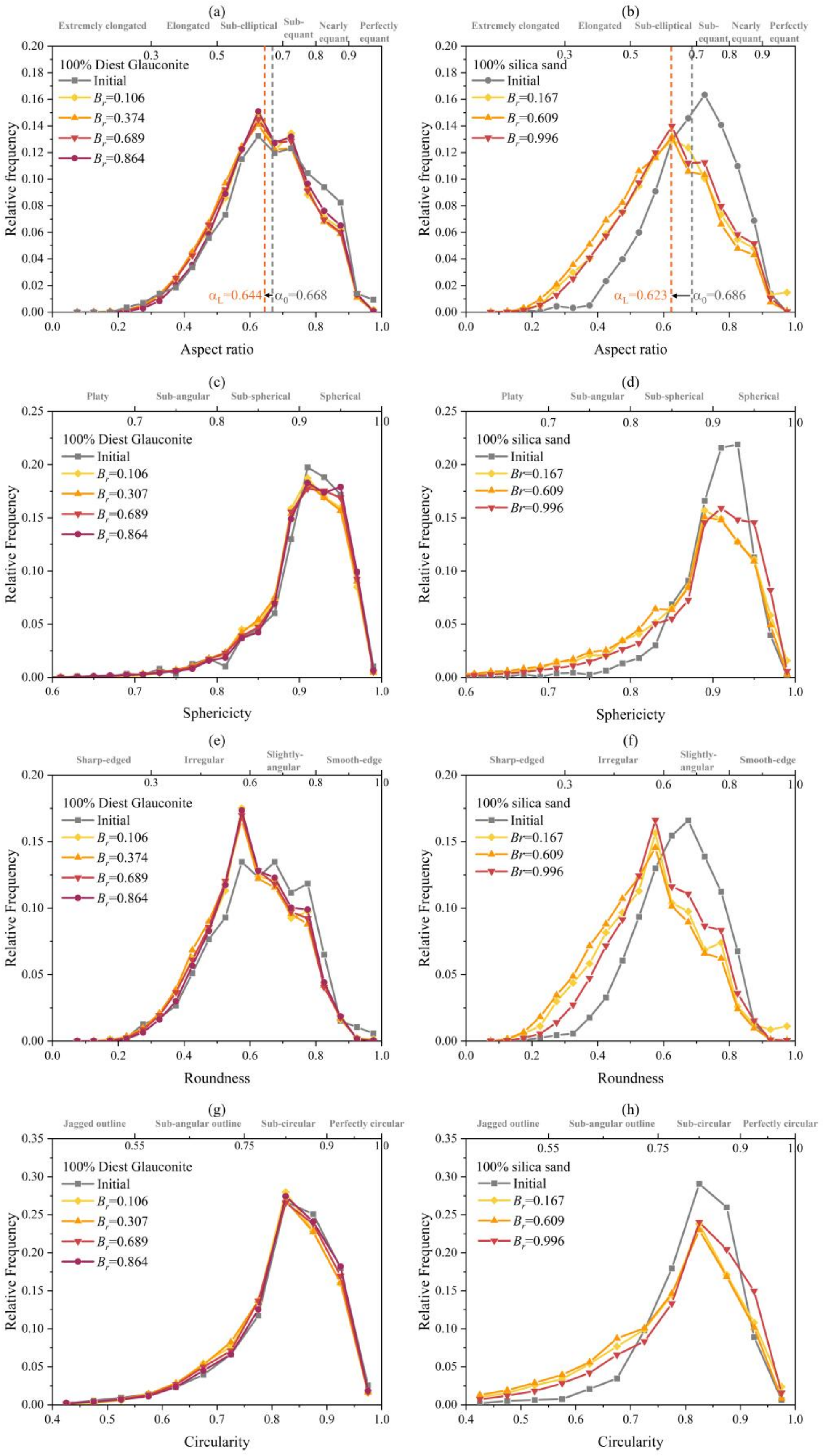

665

666 **Fig. 20.** Relative frequency distributions of (a-b) aspect ratio, (c-d) sphericity, (e-f) roundness, and (g-h) circularity

for 100% Diest Glauconite and 100% silica sand at different levels of relative breakage. The classification labels at the top of each subplot indicate the qualitative categories associated with the corresponding parameter ranges.

4. Discussion

A programme of 1D oedometric compression tests have been performed on pure glauconite sands, glauconite-silica sand mixtures and pure silica sand to systematically characterise their mechanical response and breakage behaviour. The arrested loading-unloading approach, combined with detailed particle size and shape analyses, enables direct observation of particle-scale evolution and supports the development of quantitative relationships linking breakage to macroscopic response.

The stress-strain behaviour of two types of pure glauconite sands, glauconite-silica sand mixtures and pure silica sand has been compared systematically for the first time under 1D compression. The results demonstrate a strong role of glauconite content in controlling sand crushing and compressibility. Increasing glauconite content leads to reduced stiffness, lower yield stress, and diminished energy absorption capacity. Both yield stress and work input at yielding follow clear power-law relationships with glauconite content (R^2> 0.92), highlighting its dominant influence on strength and energy absorption capacity (Fig. 8). In addition, saturated glauconite exhibits pronounced time-dependent and clay-like behaviour, with water reducing strength and energy capacity far more significantly than in silica sand. This high-water sensitivity is consistent with hydration-induced weakening and clay release, which disrupt the granular skeleton. This strong water sensitivity aligns with findings that hydration promotes glauconite disaggregation and the release of clay minerals, weakening the granular skeleton and reducing particle strength (Westgate et al., 2023).

Particle size evolution follows the well-established fractal crushing paradigm, with PSDs progressively converging toward a fractal distribution. The observed increase in fractal dimension D_s, together with its asymptotic tendency toward material-dependent ultimate values D_{su}, is consistent with observations on quartz and carbonate sands subjected to high compressive stresses (McDowell et al., 1996; Coop et al., 2004; Russell, 2011; Xiao et al., 2016; Huang et al., 2017). What distinguishes the present work is the explicit quantitative links between B_r, D_s, and specific work W. Although previous studies have linked B_r to either D_s or input energy (Huang et al., 2014, 2017; Xiao et al., 2019), they have seldom demonstrated mutually consistent relationships. The B_r and D_s relationship established in this study provide a compact descriptor of PSD evolution that links a widely used engineering index (B_r) with a physically grounded grading descriptor (D_s). When combined with the observed D_s-W and B_r-W trends, these results form a unified experimental framework that captures how strength, grading, breakage, and energy dissipation co-evolve during crushing. This framework is applicable to both glauconitic materials and conventional silica sands, and it deepens the understanding of how particle breakage progresses toward an ultimate state.

The reduction in aspect ratio, roundness, sphericity and circularity with increasing breakage is consistent with previous studies on quartz, carbonate, and calcareous sands, which show that fragmentation produces more elongated and angular particles (Buscarnera and Einav, 2021; Wei et al., 2022; Yao et al., 2023). Building on the theoretical α-B_r relationship proposed by Buscarnera and Einav (2021), the present results demonstrate that this mathematical work can be extended to capture the evolution of additional shape descriptors, namely roundness, sphericity, and circularity (Fig. 19). These shape changes have important implications for engineering behaviour. Rorato et al. (2021) showed that particle sphericity is directly related to rolling resistance and, consequently, to macroscopic frictional response. In this study, for example, sphericity decreases from 0.899 to 0.884 for 100%

silica sand, corresponding to an increase in rolling resistance coefficient from 0.51 to 0.59. This change may lead to an increase in peak strength of approximately 7.4% (Li and Smith, 2023).

Particle shape evolution further reveals mineral-dependent breakage mechanisms. Pure silica sand develops stronger elongation and irregularity than pure glauconite at equivalent or comparable strain, despite its higher macroscopic strength. This demonstrates that mineralogy governs not only the rate of PSD evolution but also the pathways of shape transformation, a feature rarely quantified in earlier breakage studies.

By integrating stress-strain behaviour, work input, particle size and shape evolution, this study establishes a unified experimental-analytical framework (Fig. 21) linking particle-scale breakage to macroscopic strength, compressibility, and energy dissipation. This framework not only advances the fundamental understanding of glauconite sands, whose breakage behaviour remains insufficiently documented in engineering practice, but also provides an experimental basis for developing analytical tools that must incorporate grading evolution, particle morphology, and mineral-dependent breakage mechanisms. Future research may extend this framework to more complex loading conditions, including triaxial and cyclic compression conditions relevant to offshore conditions. High-resolution 3D imaging techniques such as X-ray CT with digital volume correlation, combined with automated particle segmentation, could further elucidate how particle breakage and intra-particle structure control the bulk mechanical response. In parallel, the mechanisms through which water transforms glauconite into a clay-like material should be explored using advanced mineralogical and micro-mechanical methods, including environmental SEM, in-situ nano-indentation, and micro-CT under controlled saturation.

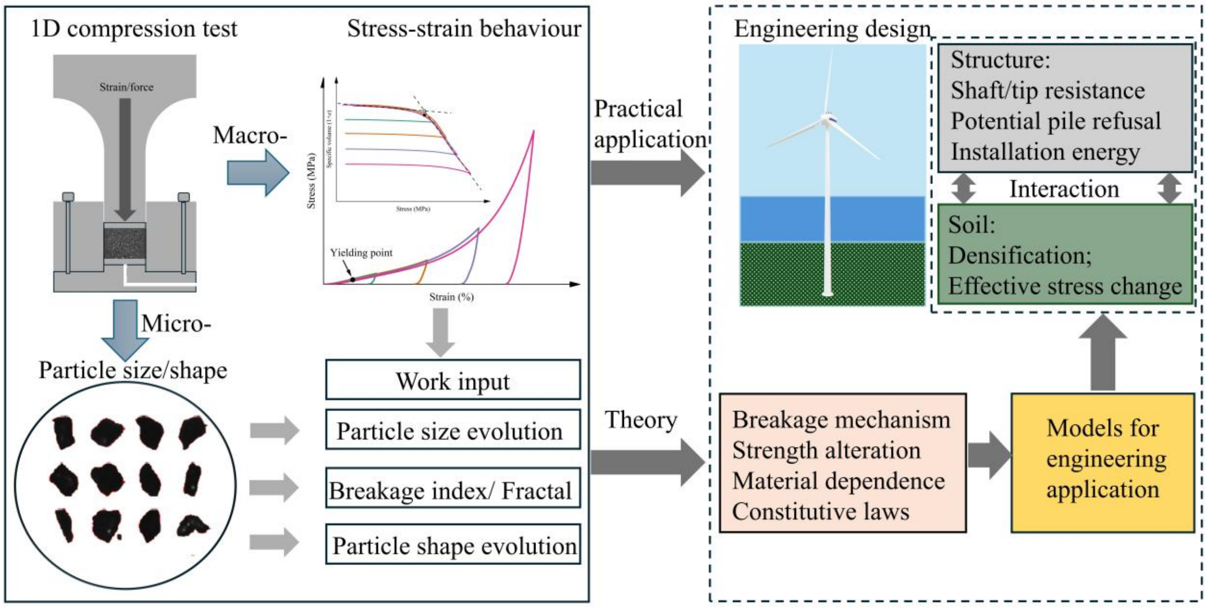

Fig. 21. Experimental and analytical framework linking 1D compression behaviour with particle-scale evolution (size, breakage, and shape) and its potential translation into geotechnical engineering applications.

5. Conclusion

This study has advanced the understanding of the role of glauconite content in controlling sand crushing and compressibility by integrating one-dimensional oedometric compression tests arrested at varying strains with high-resolution particle size and shape analysis. Sands with varying glauconite contents were examined to quantify the effects of glauconite content on yielding, particle breakage, grading evolution, and morphology. The principal findings are:

- Yielding stress and threshold work decrease significantly with increasing glauconite content, reflecting the low strength and high brittleness of glauconite grains. Power-law relationships were established between glauconite content, yielding stress, and specific work input (R^2>0.92).
- Water saturation causes a substantial reduction in the yielding stress of glauconite, dropping from 5.16-5.76 MPa (dry) to 0.45-0.47 MPa (saturated). In contrast, the influence of water on the yielding behaviour

of silica sand is relatively minor.

- All materials evolve toward finer, fractal PSDs. A robust exponential relationship was identified between relative breakage and fractal dimension, confirming fractal evolution as a reliable descriptor of particle fragmentation in glauconitic sands.
- A modified formulation captures the nonlinear relationship between relative breakage and input work, while fractal dimension asymptotically approaches a stable value with increasing energy.
- Particle shape evolution is mineral-dependent. Breakage leads to more elongated and angular particles, with silica sand showing stronger shape modification, whereas glauconite retains more equant morphologies.

CRediT authorship contribution statement

Shijin Li: Conceptualization, Methodology, Investigation, Formal analysis, Data curation, Validation, Software, Writing-original draft, Visualization; **Hannes Claes**: Resources, Investigation, Writing-review & editing; **Hadrien Rattez**: Conceptualization, Supervision, Project administration, Resources, Funding acquisition, Writing-review & editing.

Declaration of Competing interest

The authors declare that they have no competing financial interests or personal relationships that could have appeared to influence the work reported in this paper.

Acknowledgments and funding

The authors gratefully acknowledge the financial support provided by the Belgian Energy Transition Fund (ETF) through the SAGE-SAND project *"Soil Aging Around Offshore Wind Turbine Foundations - From Operational Response to Decommissioning"* (Grant No. 3E220974), and the EXCALIBUR project *"Experimental and Computational Analysis of Monopile Extraction: Leveraging Innovation and Better Understanding for Renewable offshore wind energy"*, as well as the support from the National Natural Science Foundation of China (Grant No. 52308370).

Data availability statement

All experimental data supporting the results of this study are available from the first author, Shijin Li, upon reasonable request.

Conflict of interest

The authors declare that they have no conflict of interest.

REFERECES

Adriaens, R., 2015. Neogene and Quaternary clay minerals in the southern North Sea (PhD Thesis). KU Leuven, Leuven, Belgium.

Altuhafi, F., O'Sullivan, C., Cavarretta, I., 2013. Analysis of an image-based method to quantify the size and shape of sand particles. J. Geotech. Geoenviron. Eng. 139, 1290–1307. https://doi.org/10.1061/(ASCE)GT.1943-5606.0000855.

ASTM D2435, 2020. Test methods for one-dimensional consolidation properties of soils using incremental loading. https://doi.org/10.1520/D2435.

Baldermann, A., Banerjee, S., Czuppon, G., Dietzel, M., Farkaš, J., Löhr, S., Moser, U., Scheiblhofer, E., Wright, N.M., Zack, T., 2022. Impact of green clay authigenesis on element sequestration in marine settings. Nat. Commun. 13, 1527. https://doi.org/10.1038/s41467-022-29223-6.

Barrett, E.P., Joyner, L.G., Halenda, P.P., 1951. The determination of pore volume and area distributions in porous substances. I. Computations from nitrogen isotherms. J. Am. Chem. Soc. 73, 373–380. https://doi.org/10.1021/ja01145a126.

Bellotti, R., Fretti, C., Ghionna, V.N., Pedroni, S., 1991. Compressibility and crushability of sands at high stresses, in: Proceedings of the First International Symposium on Calibration Chamber Testing. pp. 79–90.

Brunauer, S., Emmett, P.H., Teller, E., 1938. Adsorption of gases in multimolecular layers. J. Am. Chem. Soc. 60, 309–319. https://doi.org/10.1021/ja01269a023.

Buscarnera, G., Einav, I., 2021. The mechanics of brittle granular materials with coevolving grain size and shape. Proc. R. Soc. A. 477, rspa.2020.1005, 20201005. https://doi.org/10.1098/rspa.2020.1005.

Cavarretta, I., Coop, M., O'Sullivan, C., 2010. The influence of particle characteristics on the behaviour of coarse grained soils. Géotechnique 60, 413–423. https://doi.org/10.1680/geot.2010.60.6.413.

Ciantia, M.O., O'Sullivan, C., 2020. Calculating the state parameter in crushable sands. Int. J. Geomech. 20, 04020095. https://doi.org/10.1061/(ASCE)GM.1943-5622.0001707.

Coop, M.R., Sorensen, K.K., Freitas, T.B., Georgoutsos, G., 2004. Particle breakage during shearing of a carbonate sand. Géotechnique 54, 157–163. https://doi.org/10.1680/geot.2004.54.3.157.

De Nijs, R.E.P., Kaalberg, F.J., Osselaer, G., Couck, J. van, Van Royen, K., 2015. Full-scale field test (sheet) pile drivability in Antwerp (Belgium).

Dubinin, M.M., Astakhov, V.A., 1971. Development of the concepts of volume filling of micropores in the adsorption of gases and vapors by microporous adsorbents-Communication 2. General bases of the theory of adsorption of gases and vapors on zeolites. Bulletin of the Academy of Sciences of the USSR. Division of Chemical Sciences 20, 8–12.

Einav, I., 2007a. Breakage mechanics-Part II: Modelling granular materials. J. Mech. Phys. Solids 55, 1298–1320. https://doi.org/10.1016/j.jmps.2006.11.004.

Einav, I., 2007b. Breakage mechanics-Part I: Theory. J. Mech. Phys. Solids 55, 1274–1297. https://doi.org/10.1016/j.jmps.2006.11.003.

Emidio, G.D., Verástegui Flores, R.D., Van Impe W.F., 2009. Crushability of granular materials at high stress levels, in: Proceedings of the 17th International Conference on Soil Mechanics and Geotechnical Engineering. IOS Press. https://doi.org/10.3233/978-1-60750-031-5-127.

Eshel, G., Levy, G.J., Mingelgrin, U., Singer, M.J., 2004. Critical evaluation of the use of laser diffraction for particle-size distribution analysis. Soil Science Soc of Amer J 68, 736–743. https://doi.org/10.2136/sssaj2004.7360.

Fobe, B., 1995. Lithostratigraphy of the Vlierzele Formation (Ypresian, NW Belgium). Bulletin de la Societe beige de Geologie 104, 133–149.

Fobe, B., 1997. Review of the lithostratigraphy of the middle Eocene in northern Belgium. Mededelingen van de Werkgroep voor Tertiaire en Kwartaire Geologie 34, 53–67.

Grubbs, J., Tsaknopoulos, K., Massar, C., Young, B., O'Connell, A., Walde, C., Birt, A., Siopis, M., Cote, D., 2021. Comparison of laser diffraction and image analysis techniques for particle size-shape characterization in additive manufacturing applications. Powder Technol. 391, 20–33. https://doi.org/10.1016/j.powtec.2021.06.003.

Gurvich, L., G., 1915. Acerca de la fuerza de atracción fisicoquímica. Journal of Russian Physical and Chemical Society 805–27.

Ham, T.-G., Nakata, Y., Orense, R., Hyodo, M., 2010. Influence of water on the compression behavior of decomposed granite soil. J. Geotech. Geoenviron. Eng. 136, 697–705. https://doi.org/10.1061/(ASCE)GT.1943-5606.0000274.

Hardin, B.O., 1985. Crushing of soil particles. J. Geotech. Eng. 111, 1177–1192. https://doi.org/10.1061/(ASCE)0733-9410(1985)111:10(1177).

Hossain, Z., Fabricius, I.L., Christensen, H.F., 2009. Elastic and nonelastic deformation of greensand. The Leading Edge 28, 86–88.

Houthuys, R., Adriaens, R., Goolaerts, S., Laga, P., Louwye, S., Matthijs, J., Vandenberghe, N., Verhaegen, J., 2020. The Diest Formation: a review of insights from the last decades. Geol. Belg. 23, 199–218.

Houthuys, R., Gullentops, F., 1988. The Vlierzele sands (Eocene, Belgium): A tidal ridge system. Tide-influenced sedimentary environments and facies. D. Reidel Publishing Co., Dordrecht 139–152.

Huang, J., Xu, S., Hu, S., 2014. Influence of particle breakage on the dynamic compression responses of brittle granular materials. Mech. Mater. 68, 15–28. https://doi.org/10.1016/j.mechmat.2013.08.002.

Huang, J.Y., Hu, S.S., Xu, S.L., Luo, S.N., 2017. Fractal crushing of granular materials under confined compression at different strain rates. Int. J. Impact Eng. 106, 259–265. https://doi.org/10.1016/j.ijimpeng.2017.04.021.

Jiang, H., Li, Y., Huang, Q., Xue, D., Buscarnera, G., 2026. Numerical identification of size-shape-strength attractors in sheared breakable granular materials. Comput. Geotech. 190, 107709. https://doi.org/10.1016/j.compgeo.2025.107709.

Kaasschieter, J.P.H., 1961. Foraminifera of the Eocene of Belgium. Institut royal des sciences naturelles de Belgique.

Konstantinou, M., Piedrabuena, A.R., Hellebrekers, N., Mirko Mento, Ahmed Elkadi, Ken Gavin, 2025. Geotechnical properties of a glauconite sand from Belgium, in: Proceedings of the 5th ISFOG (2025). https://doi.org/10.53243/ISFOG2025-65.

Lei, J., Arroyo, M., Ciantia, M., Zhang, N., 2024. A fracture-based discrete model for simulating creep in quartz sands. Géotechnique 1–43. https://doi.org/10.1680/jgeot.23.00068.

Li, S., Russell, A.R., Muir Wood, D., 2026. Mathematical descriptions of grading linked with prediction of mechanical consequences of suffusion. Comput. Geotech. 191, 107788. https://doi.org/10.1016/j.compgeo.2025.107788.

Li, S., Smith A., 2023. Acoustic emission and energy dissipation in soils during triaxial shearing. Comput. Geotech. 162, 105639. https://doi.org/10.1016/j.compgeo.2023.105639.

Li, X., Liu, J., Li, J., 2022. Fractal dimension, particle shape, and particle breakage analysis for calcareous sand. Bull Eng Geol Environ 81, 106. https://doi.org/10.1007/s10064-022-02585-3.

López-Quirós, A., Escutia, C., Sánchez-Navas, A., Nieto, F., Garcia-Casco, A., Martín-Algarra, A., Evangelinos, D., Salabarnada, A., 2019. Glaucony authigenesis, maturity and alteration in the Weddell Sea: An indicator of paleoenvironmental conditions before the onset of Antarctic glaciation. Sci. Rep. 9, 13580.

Manso, J., Marcelino, J., Caldeira, L., 2018. Crushing and oedometer compression of rockfill using DEM. Comput. Geotech. 101, 11–22. https://doi.org/10.1016/j.compgeo.2018.04.009.

McDowell, G.R., Bolton, M.D., 1998. On the micromechanics of crushable aggregates. Géotechnique 48, 667–679. https://doi.org/10.1680/geot.1998.48.5.667.

McDowell, G.R., Bolton, M.D., Robertson, D., 1996. The fractal crushing of granular materials. J. Mech. Phys. Solids 44, 2079–2101. https://doi.org/10.1016/S0022-5096(96)00058-0.

McDowell, G.R., De Bono, J.P., 2013. On the micro mechanics of one-dimensional normal compression. Géotechnique 63, 895–908. https://doi.org/10.1680/geot.12.P.041.

McDowell, G.R., Humphreys, A., 2002. Yielding of granular materials. Granul. Matter. 4, 1–8. https://doi.org/10.1007/s10035-001-0100-4.

Mentiki, C., Davis, J., Semertzidou, K., Abbireddy, C.O.R., Hight, D.W., Williams, D., Black, M., 2015. The geology and geotechnical properties of the Thanet sand formation. Part of Crossrail Project from Department for Transport, London.

Miura, N., Toyotoshi, Y., 1975. Effect of water on the behavior of a quartz-rich sand under high stresses. Soils Found. 15, 23–34.

Muir Wood, D., 2007. The magic of sands. Can. Geotech. J. 44, 1329–1350. https://doi.org/10.1139/T07-060.

Nakata, Y., Hyodo, M., Hyde, A.F.L., Kato, Y., Murata, H., 2001. Microscopic particle crushing of sand subjected to high pressure one-dimensional compression. Soils Found. 41, 69–82. https://doi.org/10.3208/sandf.41.69.

Nihaaj, M., Kiyota, T., Shiga, M., 2025. Changes in yield stress and Weibull breakage strength of gravel mudstone along the drying and wetting cycles. Eng. Geol. 358, 108405. https://doi.org/10.1016/j.enggeo.2025.108405.

Odin, G.S., Matter, A., 2003. De Glauconiarum Origine, in: Burley, S.D., Worden, R.H. (Eds.), Sandstone Diagenesis. Wiley, pp. 121–151. https://doi.org/10.1002/9781444304459.ch4.

Perfect, E., 1997. Fractal models for the fragmentation of rocks and soils: a review. Eng. Geol. 48, 185–198. https://doi.org/10.1016/S0013-7952(97)00040-9.

Perikleous, G., Meissl, S., Diaz, A.T., Stergiou, T., Ridgway-Hill, A., 2023. Monopile installation in glauconitic sands, in: 9th International SUT Offshore Site Investigation Geotechnics Conference Proceedings “Innovative Geotechnologies for Energy Transition.” Innovative Geotechnologies for Energy Transition, Society of Underwater Technology, pp. 132–138. https://doi.org/10.3723/JBWL5180.

Van Raak, R. 2009. Geotechnical properties of glauconite sands. Artesis Hogeschool Antwerpen, Paardenmarkt 92, 2000 Antwerpen, Belgium.

Rorato, R., Arroyo, M., Gens, A., Andò E., Viggiani G., 2021. Image-based calibration of rolling resistance in discrete element models of sand. Comput. Geotech. 131: 103929. https://doi.org/10.1016/j.compgeo.2020.103929.

Russell, A.R., 2010. Water retention characteristics of soils with double porosity. Eur. J. Soil Sci. 61, 412–424. https://doi.org/10.1111/j.1365-2389.2010.01237.x

Russell, A.R., 2011. A compression line for soils with evolving particle and pore size distributions due to particle crushing. Geotech. Lett. 1, 5–9. https://doi.org/10.1680/geolett.10.00003.

Russell, A.R., Muir Wood, D., 2009. Point load tests and strength measurements for brittle spheres. Int. J. Rock Mech. Min. Sci. 46, 272–280. https://doi.org/10.1016/j.ijrmms.2008.04.004.

Steurbaut, E., 2006. YPRESIAN. Geol. Belg. 9, 73–93.

Steurbaut, E., King, C., Matthijs, J., Noiret, C., Yans, J., Van Simaeys, S., 2015. The Zemst borehole, first record of the EECO in the North Sea Basin and implications for Belgian Ypresian-Lutetian stratigraphy. Geol. Belg. 18, 147–159.

Storti, F., Billi, A., Salvini, F., 2003. Particle size distributions in natural carbonate fault rocks: insights for non-self-similar cataclasis. Earth Planet. Sci. Lett. 206, 173–186. https://doi.org/10.1016/S0012-821X(02)01077-4.

Suescun-Florez, E., Iskander, M., Bless, S., 2020. Evolution of particle damage of sand during axial compression via arrested tests. Acta Geotech. 15, 95–112. https://doi.org/10.1007/s11440-019-00892-w.

Tedrow, J.C.F., 2002. Greensand and greensand soils of New Jersey: a review. Rutgers Cooperative Extension, NJ Agricultural Experiment Station, Rutgers, the State University of New Jersey.

Tong, X., Liang, Q., Wang, G., 2026. High-performance modelling of urban non-point-source pollutant dynamics: A full-process approach. Adv. Water Resour. 211, 105241. https://doi.org/10.1016/j.advwatres.2026.105241.

Ventouras, K., Coop, M.R., 2009. On the behaviour of Thanet Sand: an example of an uncemented natural sand. Géotechnique 59, 727–738. https://doi.org/10.1680/geot.7.00061.

Wang, T., Ma L., Wang, M., Li Z., Zhang, X., Geng, H., 2022. Effects of particle shape on dynamic mechanical behaviours of coral sand under one-dimensional compression. Eng. Geol. 2022, 106624. https://doi.org/10.1016/j.enggeo.2022.106624.

Wang, X., Weng, Y., Wei, H., Meng, Q., Hu, M., 2019. Particle obstruction and crushing of dredged calcareous soil in the Nansha Islands, South China Sea. Eng. Geol. 261, 150274. https://doi.org/10.1016/j.enggeo.2019.105274.

Wang, X., Yang, D., Liu, C., Li, M., 2026. Experimental and theoretical quantification of in-situ crushing characteristics of irregularly-shaped particles under multi-axis pressure with X-ray micro-computed tomography (μCT) and discrete element method (DEM). Powder Technol. 469, 121733. https://doi.org/10.1016/j.powtec.2025.121733.

Wei, H., Liu, H., Zhao, T., Zhang, S., Ma, L., Yin, M., Meng, Q., 2022. Particle breakage and morphology changes of calcareous sands under one-dimensional compression loading. Mar Geophys Res 43, 45. https://doi.org/10.1007/s11001-022-09507-8.

Westgate, Z. J., McMullin, C., DeGroot, D., 2022. Glauconite sand challenges for U.S. offshore wind development, in: ASME 2022 4th International Offshore Wind Technical Conference. ASME 2022 4th International Offshore Wind Technical Conference, American Society of mechanical Engineers, Boston, Massachusetts, USA, p. V001T02A002. https://doi.org/10.1115/IOWTC2022-98666.

Westgate, Z. J., Rahim, A., Senanayake, A., Pisanò, F., Maldonado, C., Ridgway-Hill, A., Perikleous, Y., De Sordi, J., Roux, A., Andrews, E., Ghasemi, P., 2024. The piling in glauconitic sands (PIGS) JIP: reducing geotechnical uncertainty for U.S. offshore wind development. Offshore Technology Conference, OTC, Houston, Texas, USA, p. D031S001R007. https://doi.org/10.4043/35483-MS.

Westgate, Z. J., DeGroot, D.J., McMullin, C., Zou, Y., Guo, D., Van Haren, S., Beemer, R.D., Zeppilli, D., Miller, K.G., Browning, J.V., 2023. Effect of degradation on geotechnical behavior of glauconite sands from the U.S. Mid-Atlantic Coastal Plain. Ocean Eng. 283, 115081. https://doi.org/10.1016/j.oceaneng.2023.115081.

Wils, L., Haegeman, W., 2014. One-dimensional compression of a crushable sand in dry and wet conditions, in: Soga, K., Kumar, K., Biscontin, G., Kuo, M. (Eds.), Geomechanics from Micro to Macro. CRC Press, pp. 1403–1408. https://doi.org/10.1201/b17395-254.

Wu, Y., Yamamoto, H., Cui, J., Cheng, H., 2020. Influence of load mode on particle crushing characteristics of silica sand at high stresses. Int. J. Geomech. 20, 04019194. https://doi.org/10.1061/(ASCE)GM.1943-

5622.0001600.

Xiao, Y., Liu, H., Chen, Q., Ma, Q., Xiang, Y., Zheng, Y., 2017. Particle breakage and deformation of carbonate sands with wide range of densities during compression loading process. Acta Geotech. 12, 1177–1184. https://doi.org/10.1007/s11440-017-0580-y.

Xiao, Y., Liu, H., Xiao, P., Xiang, J., 2016. Fractal crushing of carbonate sands under impact loading. Geotech. Lett. 6, 199–204. https://doi.org/10.1680/jgele.16.00056.

Xiao, Y., Yuan, Z., Chu, J., Liu, H., Huang, J., Luo, S.N., Wang, S., Lin, J., 2019. Particle breakage and energy dissipation of carbonate sands under quasi-static and dynamic compression. Acta Geotech. 14, 1741–1755. https://doi.org/10.1007/s11440-019-00790-1.

Yang, Y., Zhang C., Wang R., Jiang M., Tian Y., 2021. Engineering properties of the compressibility and crushing characteristics of transitional soils mixed with silicate and carbonate sands. Eng. Geol. 292, 106246. https://doi.org/10.1016/j.enggeo.2021.106246.

Yao, T., Xing, X., Li, W., 2023. Evolution of particle morphology of quartz sand during one-dimensional compression. Powder Technol. 429, 118921. https://doi.org/10.1016/j.powtec.2023.118921.

Yu, F., 2017. Characteristics of particle breakage of sand in triaxial shear. Powder Technol. 320, 656–667. https://doi.org/10.1016/j.powtec.2017.08.001.

Zhang, Y.D., Buscarnera, G., Einav, I., 2016. Grain size dependence of yielding in granular soils interpreted using fracture mechanics, breakage mechanics and Weibull statistics. Géotechnique 66, 149–160. https://doi.org/10.1680/jgeot.15.P.119.

Zhao, B., Wang, J., Andò, E., Viggiani, G., Coop, M.R., 2020. Investigation of particle breakage under one-dimensional compression of sand using X-ray microtomography. Can. Geotech. J. 57, 754–762. https://doi.org/10.1139/cgj-2018-0548.

Zou, Y., DeGroot, D.J., Westgate, Z.J., 2025. Direct and interface shear behavior of an authigenic glauconite sand from the coastal plain of New Jersey. J. Geotech. Geoenviron. Eng. 151, 04025065. https://doi.org/10.1061/JGGEFK.GTENG-13275.

Appendix

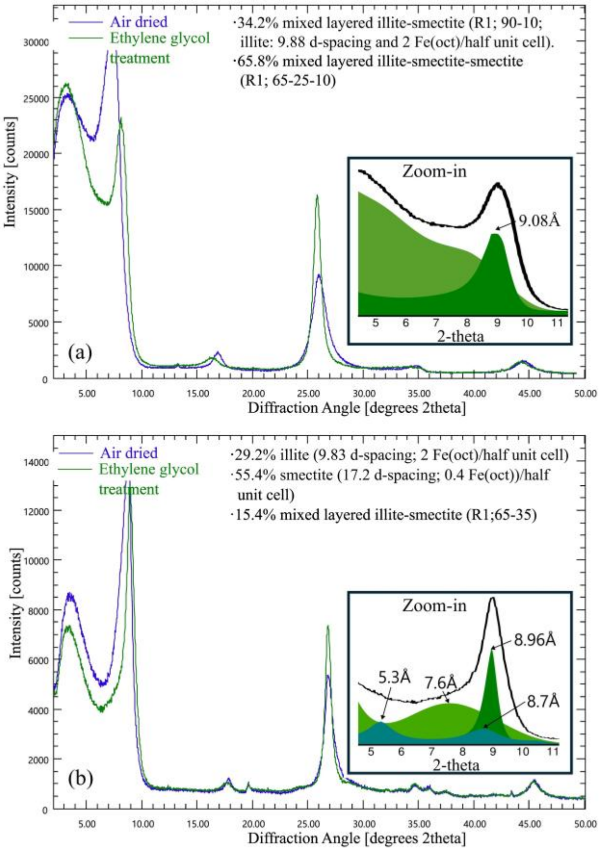

Fig.A 1. Zoom on air dried and ethylene glycolated X-Ray Diffraction intensity after Jackson clay treatment of the magnetic fraction of the glauconite-rich Vlierzele sands, for varying 2-theta. Inset shows the deconvoluted clay peaks in the zone from 5 to 11 2-theta. (a) glauconite-rich Vlierzele sands; (b) glauconite-rich Diest sands.

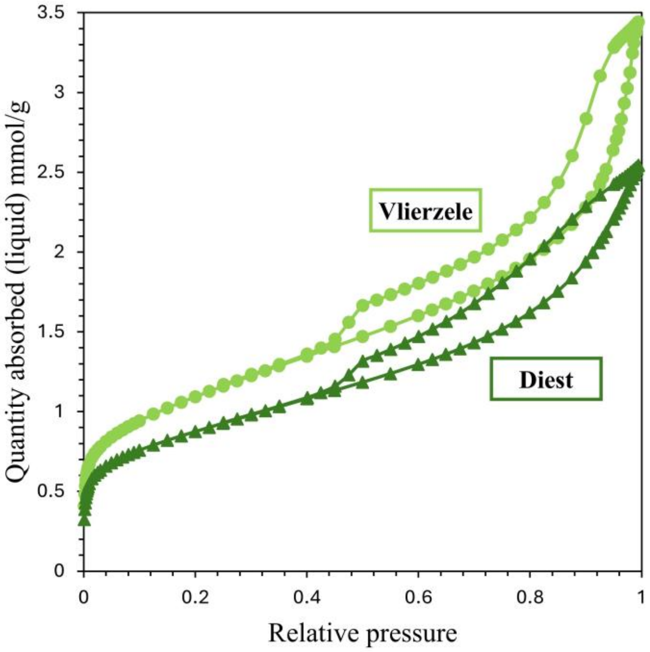

Fig.A 2. N2 physisorption isotherms of the glauconite fractions. Both samples show a type II isotherm as typical for clay materials (e.g. Seemann et al., 2025).

Fig.A. 3 (a) illustrates the stress and strain evolution during the incremental loading (IL) 1D compression test on saturated 100% Diest glauconite (Test 8). Each strain step is followed by a holding period to allow pore pressure dissipation. Fig.A. 3 (b) presents the corresponding stress-strain relationship, showing a progressive increase in stress with strain, characteristic of strain hardening. The colour scale represents the data point density, increasing from purple (low) to red (high), highlighting the time-dependent accumulation of deformation within each loading stage. When the target strain of each loading step is reached, the system records the current force and maintains it as a constant load. During this adjustment phase, one or two stress fluctuations may occur, causing an increase in strain (typically about 2.5-5%), which results in the discontinuous appearance of the stress-strain curve. Moreover, when stress is held constant, only the final loading stage exhibits noticeable time-dependent strain (also refer to Fig.A. 3 (a)), likely reflecting the clay-like behaviour of crushed glauconite under saturated conditions.

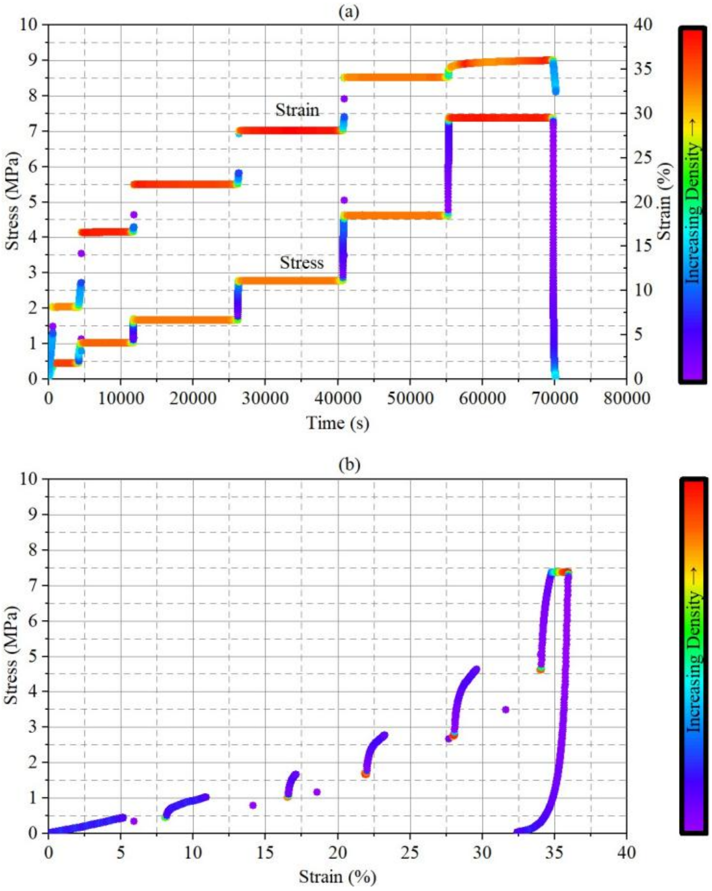

Fig.A. 3. Demonstration of incremental loading (IL) pattern. (a) stress and strain over time; (b) stress-strain. Colour scale indicates increasing data point density from purple (low) to red (high).

To better understand the mechanisms underlying the reduction in mean aspect ratio shown in Fig.19. (a), Fig.A. 4 presents the relative frequency distributions of aspect ratio α for all tested materials with varying glauconite contents. Each distribution is unimodal, with the peak generally located around α=0.6-0.72, corresponding to sub-elliptical to sub-equant particles. All materials exhibit unimodal aspect ratio distributions, with peaks consistently cantered around α=0.6-0.72. The largest change in relative frequency occurs between the initial condition and the first breakage level, indicating that particle elongation primarily develops during the early stage of fragmentation. Thereafter, the distributions remain largely stable, suggesting limited additional morphological modification with further breakage. Although glauconite is more susceptible to crushing, glauconitic grains exhibit only minor elongation, whereas silica sand shows a more pronounced elongation trend, reflecting the brittle fracture characteristics of quartz grains.

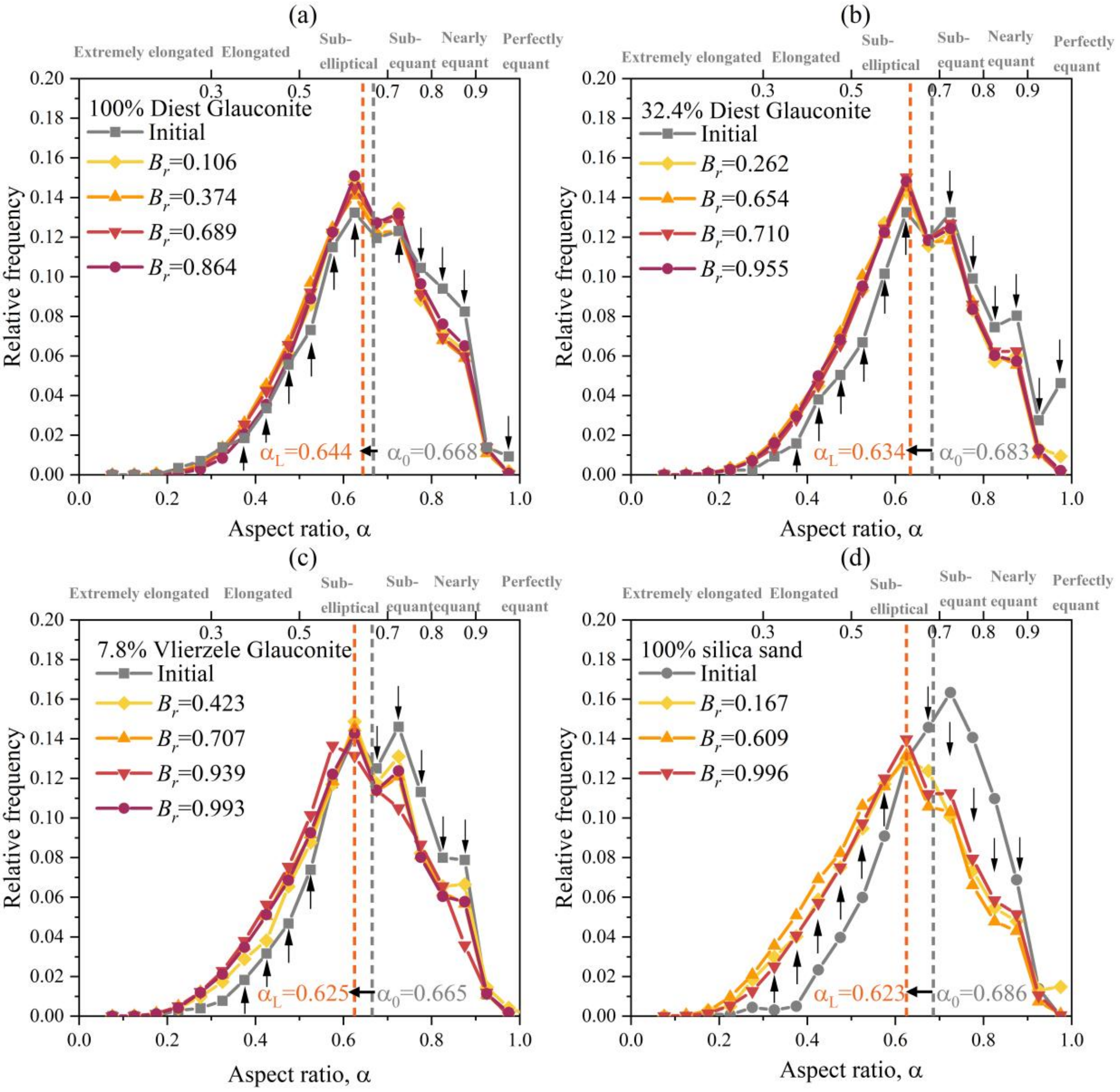

Fig.A. 4 Relative frequency distributions of particle aspect ratio for samples with varying glauconite content: (a) 100% Diest Glauconite, (b) 32.4% Diest Glauconite, (c) 7.8% Vlierzele Glauconite, and (d) 100% silica sand. The classification labels at the top of each subplot indicate the qualitative categories associated with the corresponding parameter ranges